Journal of Materials Chemistry A

ROYAL SOCIETY OF CHEMISTRY

REVIEW

View Article Online
View Journal | View Issue

Cite this: *J. Mater. Chem. A*, 2022, **10**, 19107

Understanding (photo)electrocatalysis for the conversion of methane to valuable chemicals through partial oxidation processes

Love Kumar Dhandole, Sang Hoon Kim and Gun-hee Moon *

Received 21st March 2022
Accepted 16th May 2022

DOI: 10.1039/d2ta02257e

rsc.li/materials-a

Methane (CH_4) with sp^3 hybridization is known as a main constituent of natural gas, and has been utilized as a fuel and a hydrogen reservoir for power plant and transportation applications. Along with the complete oxidation of CH_4 to CO_2 to retard global warming, the partial oxidation toward the generation of liquid fuels is a big challenge because oxygenated products are more prone to oxidation than CH_4. Therefore, the control of the charge carriers and radical species is critical to prohibit the unwanted reaction, in other words, to maximize the formation of desired products. Photo and electrocatalysis are clean and sustainable techniques for CH_4 conversion, which do not require extreme experimental conditions (*i.e.*, high temperature and pressure), and indeed, the reaction can be driven under sunlight (*i.e.*, charge carriers generated by light absorption or photovoltaic-assisted electricity). In this review, we discuss how

Extreme Materials Research Center, Korea Institute of Science and Technology (KIST), 5. Hwarang-ro 14-gil, Seongbuk-gu, Seoul 02792, Republic of Korea. E-mail: catalysis@kist.re.kr

Love Kumar Dhandole received a BE in Electronics & Communication Engineering from RGPV University (India) in 2008, an MTech degree in Green Energy Technology from Pondicherry University (India) in 2014, while working as a Master project student in International Advanced Research Centre for Powder Metallurgy and New Materials R&D (ARCI, Hyderabad, India), and a PhD degree from the Dept of BioTechnology, Chonbuk National University (Iksan campus, Korea) in 2018 under the guidance of Prof. Jum Suk Jang. After brief postdoctoral stints in Chonbuk National University, he joined his second postdoctoral position at the EcoFriendly Catalysis & Energy Lab., under the supervision of Prof. Jae Sung Lee in Dept of Energy Engineering, School of Energy and Chemical Engineering, Ulsan National Institute of Science and Technology (UNIST), Ulsan, in 2019, where he worked on visible light photoanode materials for water oxidation and hydrogen evolution applications. After his second postdoctoral, he moved to the Korea Institute of Science and Technology (KIST), Seoul, where he is currently a postdoctoral candidate working on the design of photocatalysts, photoelectrochemical cells, and carbon materials for energy conversion and environmental applications.

Dr Sang Hoon Kim received his doctoral degree from Institute of Physics, Humboldt University of Berlin, Germany in 2003 while working as a research associate and doctoral student in Physical Chemistry Department at the Fritz Haber Institute of the Max Planck Society, Berlin, Germany. After brief postdoctoral stints in Materials Sciences Division at Lawrence Berkeley National Laboratory and in Department of Materials Science and Engineering at University of Pennsylvania, he joined the R&D division of Hitachi Global Storage Technologies in San Jose, CA, USA in 2006, working for the development of next-generation hard disk drives. In 2011, he joined Korea Institute of Science and Technology as Senior Research Scientist and in 2016, he was promoted to Principal Research Scientist.

to design catalysts to overcome the bottlenecks in the photo and electrocatalytic partial oxidation of CH_4 with focus on (i) an interfacial charge transfer process, (ii) strategies for surface engineering of catalysts, (iii) key factors affecting the reaction mechanism and rate-determining step, and (iv) a systematic investigation of the reaction conditions to lift up the catalytic performance. Finally, we propose the milestone to guide not only the preparation of catalysts that can effectively generate charge carriers and intermediates with a mild oxidation behavior but also the design of reactors for scale-up to prevent undesired reaction pathways.

1. Introduction

Depending on the aspect of climate change and energy crisis, the conversion of methane (CH_4), the largest component of natural gas (70–90%), should lead toward the complete oxidation to carbon dioxide (CO_2) and partial oxidation to valuable oxygenates and (halo)hydrocarbons, respectively. With an environmental perspective, CH_4 is considered as one of the greenhouse gases, whose global warming potential (GWP, a measure of how much heat is trapped by each greenhouse gases in the atmosphere relative to CO_2) is 25 times higher than that of CO_2 over a 100 year period.[1] Indeed, CH_4 is a major source for rising tropospheric ozone level, damaging human health and plant growth.[2,3] Therefore, many countries pledged to cut CH_4 emission by 30% by 2030 under the Paris agreement. CH_4 emission occurs from both nature and human activities, and the main sources in the latter are natural gas harvesting, petroleum industry, enteric fermentation, landfills, manure management, and coal mining (Fig. 1a).[4] Due to the inevitable emission of CH_4, concerted efforts to cut it down in agriculture and industry has been made for achieving the goals of the climate agreement. From an energy security standpoint, the discovery of a vast storehouse of methane hydrate as well as the advance of gas-well drilling and hydraulic fracturing technologies make CH_4 more readily available in the exothermic combustion of vehicular fuels and thermal power generation.[5] The production of liquid hydrocarbons and oxygenates through the conversion of CH_4 is of major interest due to it being more useable as a basic building block for manufacturing diverse products, a high volumetric energy density (*e.g.*, 37.8 J L^{-1} for CH_4 *versus* 17.8 MJ L^{-1} for methanol at 15 °C under 1 bar), and relatively low transportation/storage cost as well.[6] Accordingly, it has received attention to develop low-cost, ecofriendly, and highly-efficient methods for the direct conversion of CH_4 to desired compounds.

CH_4 with sp^3 hybridization is known as a stable molecule in terms of the intrinsic inertness for C–H activation; thus, an energy intensive step requiring a high temperature and pressure is required to convert it to the desired products. In the industry, the steam methane reforming process ($CH_4(g) + 0.5O_2(g) \rightarrow CO(g) + 2H_2(g)$; $CH_4(g) + H_2O(v) \rightarrow CO(g) + 3H_2(g)$) operating at 700–1000 °C and 3–25 bar generates hydrogen (H_2) and carbon monoxide (CO), which are utilized as not only fuel in fuel cell vehicle but also precursors to synthesize a wide range

Gun-hee Moon received a BS degree in Chemical Engineering from Inha University (Incheon, Korea) in 2008, an MS degree in Environmental Engineering from POSTECH in 2011, and a PhD degree in Chemical Engineering from POSTECH (Pohang, Korea) in 2015. During the PhD course, he joined as a visiting student at the Pacific Northwest National Laboratory (PNNL, 2011.06–2012.05). He started his first postdoctoral career at the Institute of Environmental and Energy Technology in POSTECH (2015.03–2016.08) and accumulated research experience at The Institute of Science and Industrial Research (SANKEN), Osaka University (2016.06–2016.07). After his second postdoctoral stay at the Max-Planck-Institut für Kohlenforschung (Germany, 2016.09–2020.10), he moved to the Korea Institute of Science and Technology (KIST), where he is currently employed as a senior scientist working on the design of photocatalysts, electrocatalysts, photoelectrochemical cells, and carbon materials for energy conversion and environmental applications.

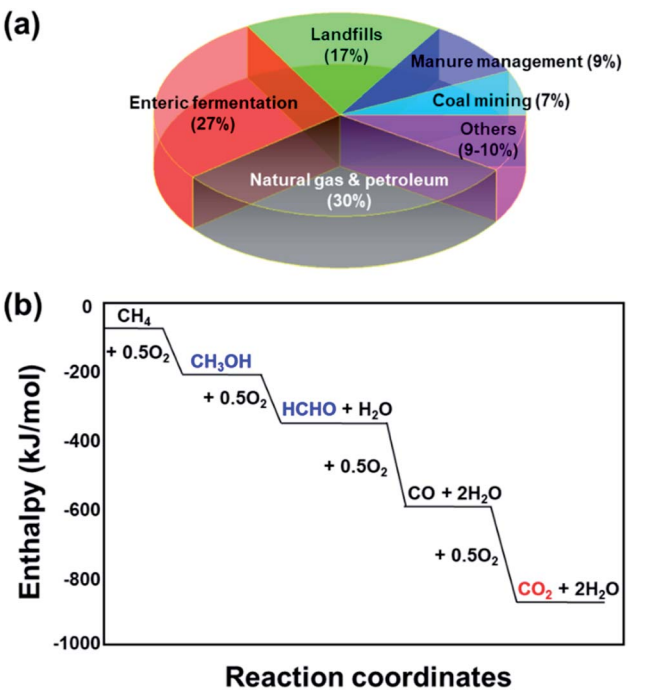

Fig. 1 (a) Source of methane emission in U.S. in 2019. (b) Enthalpy change of the sequential oxidation of CH_4 at 298 K. Redrawn with permission.[9] Copyright 1991, Elsevier.

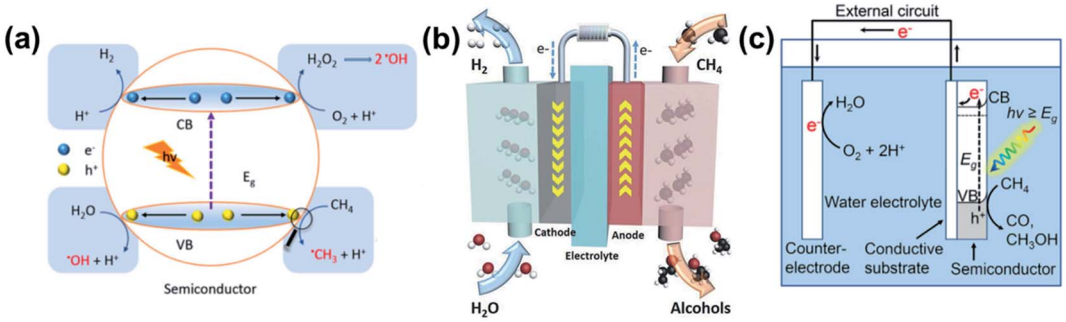

Fig. 2 Schematic diagram of (a) photocatalysis, (b) electrocatalysis, and (c) photoelectrochemical cell for the oxidation of CH_4. Reproduced with permission.[77,114,115] Copyright 2019 and 2021, Elsevier. Copyright 2017, Wiley.

of chemicals and polymers.[7,8] In order to produce value-added chemicals and fuels *via* the direct conversion of CH_4, reaction with a limited amount of oxygen (*i.e.*, partial oxidation with less than the stoichiometric oxygen content) should be employed for prohibiting the oxidation of CH_4 into CO_2 and H_2O ($CH_4(g) + 2O_2(g) \rightarrow CO_2(g) + 2H_2O(v)$, $\Delta H^\circ_{298} = -802.6$ kJ mol^{-1}). However, it is unavoidable that a huge amount of CO_2 is released as a byproduct, and the process is not energetically favorable relative to complete oxidation (*e.g.*, $CH_4(g) + 0.5O_2(g) \rightarrow CH_3OH(g)$, $\Delta H^\circ_{298} = -126.4$ kJ mol^{-1}; $CH_4(g) + O_2(g) \rightarrow HCHO(g) + H_2O(v)$, $\Delta H^\circ_{298} = -276$ kJ mol^{-1}) (Fig. 1b).[9]

Photo and electricity-assisted conversion of CH_4 to valuable chemicals and liquid fuels is a future-oriented technology since the reaction proceeds under mild conditions (*i.e.*, room temperature and atmospheric pressure) and renewable energy stemming from sunlight, wind, biomass, *etc.*, is likely to replace fossil fuels. Moreover, the system does not require a complex and centralized infrastructure, which makes it suitable for remote location applications such as offshore drilling rigs, shale gas extraction facilities, and landfills. On the other hand, the bottleneck in the partial oxidation process of CH_4 mainly comes from a poor selectivity toward the target products as well as low reactivity owing to the activation energy barrier. The physicochemical property of CH_4, including a high homolytic bond dissociation energy for H-abstraction (440 kJ mol^{-1}), weakly-polarized symmetric sp^3 geometry, weak acidity, and poor solubility should be considered to develop active catalysts.[10–12] Given the relatively effective dissociation behavior of CH_4 in thermocatalysis,[13,14] a wide range of transition metal-based catalysts such as zerovalent metals, metal oxides, metal complexes, single metal atoms, and metal-exchanged zeolites have been revisited to be utilized as photo, electro, or cocatalysts. Furthermore, as part of methodologies to overcome such a high energy barrier, the addition of hydrogen peroxide (H_2O_2) enables the formation of hydroxyl radicals ($^\bullet$OH) with a strong oxidation power ($E^\circ(OH/OH^-) = 1.90$–2.70 V_{NHE}).[15]

In photocatalysis, electrons and holes generated under the illumination of UV or visible light can initiate the oxidation of CH_4, which can be controlled by the electronic structure of semiconducting materials and the operation parameters (*e.g.*, light intensity and wavelength, pH, and dissolved oxygen concentration) (Fig. 2a). Without the intervention of photocatalysts, the direct irradiation with wavelength below 140 and 98.3 nm initiates the excitation of CH_4 by the electronic transition ($CH_4(g) + h\nu \rightarrow CH_4^*(g)$) and the ionization of CH_4 ($CH_4(g) + h\nu \rightarrow CH_4^+(g) + e^-$), respectively.[16] When the valence band potential of photocatalysts is deep enough to oxidize CH_4, the hole-mediated reaction occurs. Gauging the radical-involved process in aqueous media, two main paths produce $^\bullet$OH: (i) a reductive pathway mediated by electron transfer, 1st: $O_{2,dissolved} + H^+ + e^- \rightarrow HO_2(aq)$, 2nd: $HO_2(aq) + H^+ + e^- \rightarrow H_2O_2(aq)$, 3rd: $H_2O_2(aq) + e^- \rightarrow OH^- + {}^\bullet OH$, and (ii) an oxidative pathway mediated by hole transfer: $OH^- + h^+ \rightarrow {}^\bullet OH$.[17–19] The non-selective $^\bullet$OH directly attacks CH_4 and consequently facilitates its partial and complete oxidation depending on the experimental conditions. In photocatalysis, photogenerated electron–hole pairs are manipulated within one particle, whose conduction/valence band position thermodynamically determines whether an interfacial charge transfer occurs or not. However, in electrocatalysis, the driving force can be controlled by applying the potential, where the reduction and oxidation reactions are separated by a membrane (Fig. 2b). The problems associated with poor mass transfer and low solubility of CH_4 should be avoided to optimize the cell performance. In this regard, a membrane electrode assembly (MEA) with outperforming typical H-type cells is suggested, where each cathode and anode catalyst layer is coated on the front and back side of a separator or membrane, respectively.[20] The gas diffusion layer (GDL) coated on the outside of the catalyst layers dramatically improves the mass transport limitation of CH_4 and gas phase products.[21] Furthermore, the overoxidation can be avoid by the set-up of the flow cell that is able to collect liquid oxygenates from the electrolyte. When designing anode catalysts, it is critical to selectively oxidize CH_4 instead of oxygenate products. Indeed, the competitive oxygen evolution reaction and the performance deterioration caused by ohmic, mass transport, and kinetic losses should be under control, especially when the cell voltage or the current density is high.[22] For example, to meet the economic viability for the conversion of CH_4 to methanol, the selectivity should be at least 70% under the conditions (the overpotential <1 V and the current density >100 mA cm^{-2} at 100–250 °C).[23] A photoelectrochemical (PEC) cell is a combined system of photocatalysis and electrocatalysis; the operation is possible under bias-free conditions (*i.e.*,

without electricity) and the oxidation/reduction reaction can be separated *via* the proper configuration of cells (Fig. 2c). Because of the deep valence band position of O_{2p} and N_{2p} in metal oxides and nitrides, respectively, photogenerated holes with strong oxidation power are feasible to stimulate the oxidation of CH_4. Under an applied external bias or using a tandem PEC cell, a prolonged lifetime of charge carriers is achieved as a result of the band bending of the depletion layer, hence increasing the driving force for interfacial hole transfer to CH_4.

In this review, we overview the state-of-the-art strategies that have been well established for the partial oxidation of CH_4 by means of photocatalysis, electrocatalysis, PEC cells, and advanced oxidation process (AOP)-related radical reaction, and discuss the geometric and electronic parameters of catalysts, reactor engineering, and the effect of the surroundings contributing to the activity and selectivity. Understanding the mechanistic pathway of electron- and hole-mediated reactions correlated with the formation of intermediates and products will offer a rational solution to overcome the bottleneck and optimize the catalytic performance as well. Rather than describing the synthesis of new materials and their characterizations, we focus on the surface engineering of catalysts affecting the interfacial charge transfer processes in the microenvironment and key factors changing the reaction mechanism and rate-determining step. At the end, we outline the milestones to lead researchers into the right path for not only the design of promising catalysts but also the engineering of reactors for scale-up.

2. Mechanistic view for methane conversion to desired products

As CH_4 is pyrolyzed above 700 °C, hydrocarbons can be produced by autocatalysis following the sequential processes ($CH_4 \rightarrow C_2H_6 \rightarrow C_2H_4 \rightarrow C_2H_2 \rightarrow$ aromatic hydrocarbons and coke), which is initiated by the radical species ($CH_4 \rightarrow CH_3^{\bullet} + H^{\bullet}$).[24] Likewise, C_2 and C_3 products are obtained by the chain propagation (*e.g.*, $2CH_3^{\bullet} \rightarrow C_2H_6$; $CH_3^{\bullet} + C_2H_6 \rightarrow C_2H_5^{\bullet} + CH_4$; $C_2H_5^{\bullet} \rightarrow C_2H_4 + H^{\bullet}$; $CH_3^{\bullet} + C_2H_4 \rightarrow C_2H_3^{\bullet} + CH_4$; $C_2H_3^{\bullet} \rightarrow C_2H_2 + H^{\bullet}$ for C_2 hydrocarbons and $CH_3^{\bullet} + C_2H_4 \rightarrow n\text{-}C_3H_7^{\bullet}$; $n\text{-}C_3H_7^{\bullet} \rightarrow C_3H_6 + H^{\bullet}$; $CH_3^{\bullet} + C_3H_6 \rightarrow C_3H_5^{\bullet} + CH_4$; $C_3H_5^{\bullet} \rightarrow C_3H_4 + H^{\bullet}$ for C_3 hydrocarbons). In the presence of O_2, diverse oxygenates can also be generated by both $CH_3^{\bullet}$ and $OH_2^{\bullet}$ radicals ($CH_4 + O_2 \rightarrow CH_3^{\bullet} + OH_2^{\bullet}$), which are involved in the formation of acetic acid, methanol, formaldehyde, *etc.* (*e.g.*, $CH_3^{\bullet} + O_2 \leftrightarrow CH_3O_2^{\bullet}$; $CH_3O_2^{\bullet} + CH_4 \rightarrow CH_3COOH + CH_3^{\bullet}$; $CH_3O_2^{\bullet} + CH_4 \rightarrow CH_3OH + CH_3O$; $CH_3O_2^{\bullet} \rightarrow HCHO + OH^{\bullet}$).[25] However, the problem is that the yield is extremely low.

The introduction of oxidants (*e.g.*, nitrogen oxide, H_2O_2, O_2, and water) or/and heterogeneous catalysts sheds light on the solution to enhance the yield and selectivity since the activation energy can be effectively reduced. For example, the reactive radical species ($CH_3^{\bullet}$, $CH_3O^{\bullet}$, *etc.*) can appear through the attack of nitrogen dioxide (NO_2) (*e.g.*, $CH_4 + NO_2 \rightarrow CH_3^{\bullet} + HNO_2$; $CH_3^{\bullet} + NO_2 \rightarrow CH_3O^{\bullet} + NO$). Over the surface of heterogeneous catalysts at low temperature, it is proposed that

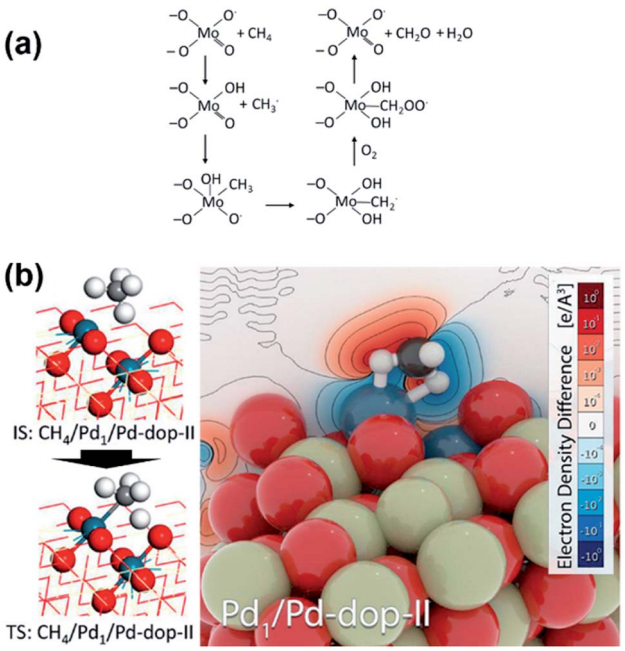

Fig. 3 (a) Partial oxidation of CH_4 into formaldehyde by electrophilic oxygen atoms (M–O sites) over molybdenum oxide. (b) Adsorption and transition states of CH_4 on Pd-doped CeO_2 and electron density map (cyan = Pd; red = O; off-white = Ce; gray = C; white = H). Reproduced with permission.[116] Copyright 2018, American Chemical Society.

the C–H bond is cleaved by two mechanistic pathways. One is dehydrogenation involving electrophilic oxygen atoms (M–O sites) as a result of the formation of $CH_3^{\bullet}$ by H-abstraction (Fig. 3a). The other is deprotonation stemming from the dissociative adsorption of CH_4 (*i.e.*, $CH_4 \rightarrow CH_3^- + H^+$) following an instant coordination onto unsaturated metal centers to form the M–C σ-bond (Fig. 3b).[26] The former is a radical-mediated oxidation process with a formal oxidation state (FOS) of C^{-III} for CH_4 (*i.e.*, 1st: $M + 0.5O_2 \rightarrow$ M–O for the formation of active site; 2nd: $M\text{–}O + CH_4 \rightarrow M\text{–}O\cdots CH_4$ with sp^2 trigonal geometry $\rightarrow$ M–OH + $CH_3^{\bullet}$ for the activation of CH_4). In the latter, the direct cleavage of CH_4 occurs from the complexation with atomic metals accompanied by an FOS of C^{-IV} for CH_4 (*i.e.*, $M + CH_4 \rightarrow H^+ + M\text{–}CH_3$ with sp^3 tetragonal geometry). As for the dehydrogenation process, the formation of the M–O active site and the C–H activation should be kinetically balanced to optimize the performance of the catalysts. Photo and electrocatalysis over transition metal oxides can assist the (re)generation of active sites on the catalyst surface. In regard to the deprotonation process, the presence of proton acceptors on the surface of catalysts facilitates the reaction kinetics, and surface oxidizing M–O species that are able to be formed by photo and electrocatalysis may play an important role as a proton acceptor.

The study of CH_4 conversion in heterogeneous photocatalysis has mainly focused on gas phase systems, where the overoxidation of CH_4 was caused by the lattice and surface adsorbed oxygens, which consequently led to the formation of CO and CO_2. The cleavage of the C–H bond initiated by the

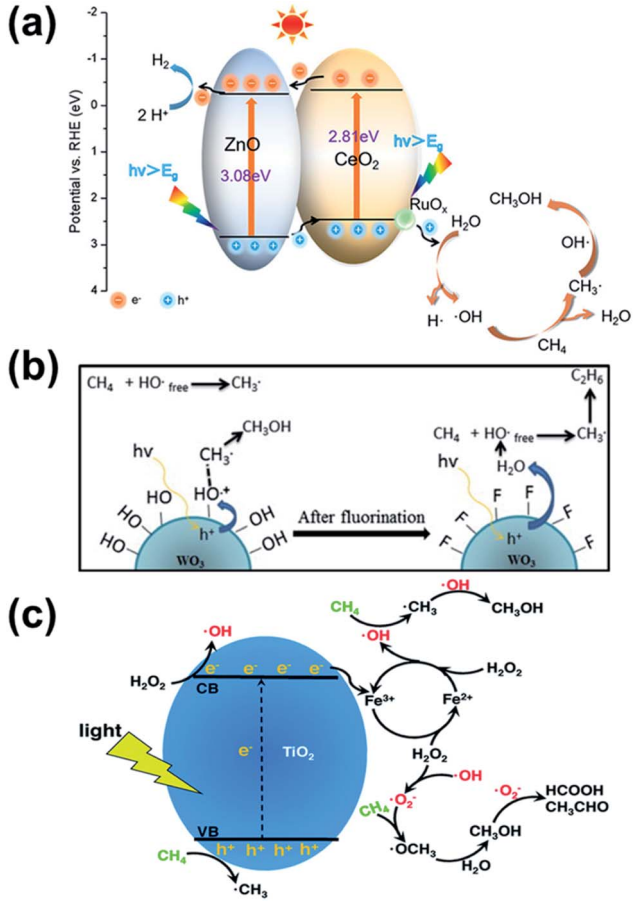

Fig. 4 (a) Mobile ˙OH-mediated CH_4 oxidation pathway over the 0.30% $RuO_x/ZnO/CeO_2$ composite. Reproduced with permission.[31] Copyright 2022, American Chemical Society. (b) Change of the reaction pathway for CH_4 oxidation before and after the surface fluorination of WO_3. While the surface bound ˙OH produces methanol, mobile ˙OH prefers to generate ethane. Reproduced with permission.[32] Copyright 2015, Elsevier. (c) Partial oxidation of CH_4 by reactive oxygen species including mobile ˙OH formed through the photo-Fenton process. Reproduced with permission.[34] Copyright 2020, Royal Society of Chemistry.

trapped hole (M^{z+}–O^{2-} + h^+ → M^{z+}–O^{-}˙ in metal oxides), ˙OH, or other electrophilic oxygen species is crucial for the partial oxidation. In contrast, the formation of reactive oxygen species (ROS) should be minimized in order to increase the selectivity for the non-oxidative coupling of CH_4.[26] As such, the manipulation of proper oxidants and radical species determines whether to synthesize oxygenates or hydrocarbons as the final products. In an aqueous system, the activation of CH_4 may be more favorable by mobile ˙OH rather than by the trapped hole (or surface bound ˙OH) in that the solubility of CH_4 is extremely low and the adsorption of CH_4 on the surface of catalysts is difficult under mild conditions (Fig. 4a).[27–31] The opposite outcome was also reported, *i.e.*, mobile ˙OH stimulates the formation of C_2H_6, whereas the reaction of surface-bound ˙OH with CH_3˙ selectively produces methanol (Fig. 4b).[32] The true mechanism of photocatalytic CH_4 conversion is still a mystery. Nevertheless, it should be noted that the handling of time-dependent ˙OH concentration is important to improve the catalytic performance. The design of flow-type reactors is one of the strategies for not accumulating the oxidative radical species (*i.e.*, to prevent overoxidation).[33] In addition, the photo-Fenton process is another approach to supply ˙OH in terms of the activation of H_2O_2 ($Fe^{3+} + e^- \rightarrow Fe^{2+}$; $Fe^{2+} + H_2O_2 \rightarrow Fe^{3+} + {}^{\cdot}OH + OH^-$) (Fig. 4c).[34,35] In spite of much efforts, the issue that the relatively high quantum yield and selectivity are obtained when the conversion of CH_4 is extremely low is still unsolved in photocatalysis.

The electrocatalytic conversion of CH_4 to value-added chemicals is driven by an anodic pathway, where active sites generated by applying positive bias ($M–O^{2-} \rightarrow M–O + 2e^-$ or

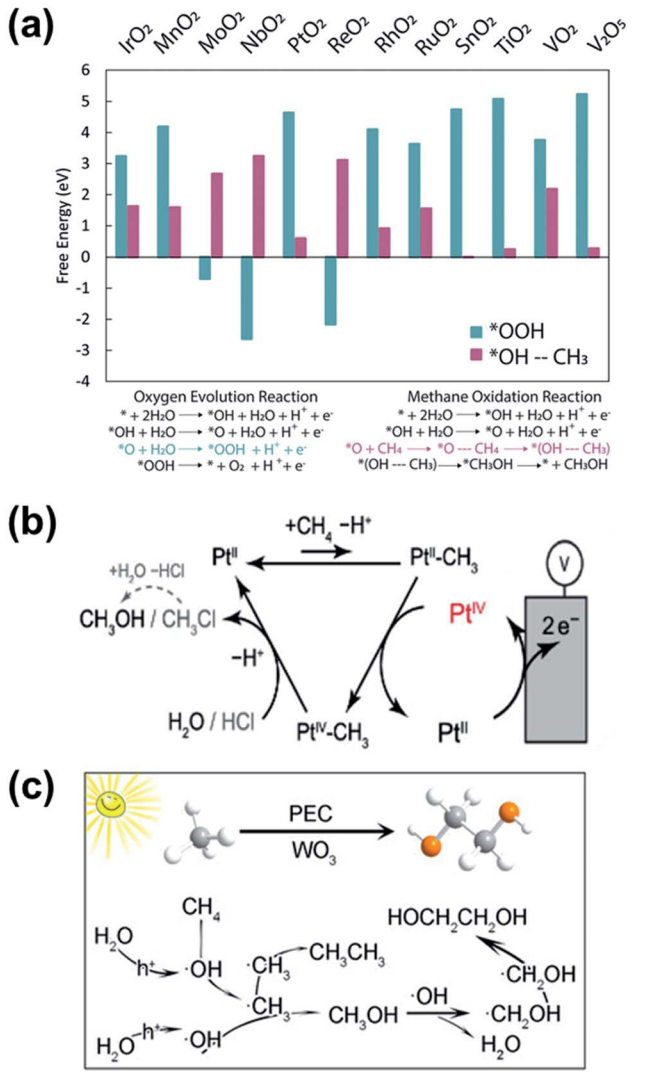

Fig. 5 (a) Comparison of the Gibbs free energy of transition metal oxide catalysts calculated from water oxidation (O* + H_2O → *OOH + H^+ + e^-) and CH_4 activation (O* + CH_4 → *O–CH_4 → *(HO–CH_3)). Reproduced with permission.[20] Copyright 2020, American Chemical Society. (b) Catalytic cycle of CH_4 conversion to methanol or methyl chloride mediated by electrochemically regenerated $[Pt^{IV}Cl_6]^{2-}$. Reproduced with permission.[41] Copyright 2020, American Chemical Society. (c) Reaction pathway to form ethylene glycol on the WO_3 photoanode. Reproduced with permission.[42] Copyright 2021, Wiley.

$MO_x + H_2O \rightarrow MO_x(^{\bullet}OH) + H^+ + e^-$; $MO_x(^{\bullet}OH) \rightarrow MO_x{-}O + H^+ + e^-$) oxidizes CH_4. Along with the applied electrode potential, the local chemical environment influenced by adsorbates, supports, electrolyte constitutes, 3D chemical surroundings, temperature, pressure, *etc.*, would also change the CH_4 oxidation process.[36] The oxygen evolution reaction (OER) is a predominant process when a high voltage is applied for transition metal oxide catalysts such as Co_3O_4, NiO, and RuO_2,[37–39] which is known as a competitive reaction for the oxidation of CH_4 in aqueous media. Fig. 5a compares the Gibbs free energy of transition metal oxides for water oxidation ($O^* + H_2O \rightarrow {}^*OOH + H^+ + e^-$) and CH_4 activation ($O^* + CH_4 \rightarrow {}^*O{-}CH_4 \rightarrow {}^*(HO{-}CH_3)$).[22] Through the reaction steps, molecular oxygen ($^*OOH \rightarrow {}^* + O_2 + H^+ + e^-$) and methanol ($^*(HO{-}CH_3) \rightarrow {}^*CH_3OH \rightarrow {}^* + CH_3OH$) are produced as the final product. In both the reactions, the dehydrogenation of *OH ($^*OH \rightarrow {}^*O + H^+ + e^-$) that is formed by single electron transfer process ($^* + H_2O \rightarrow {}^*OH + H^+ + e^-$) creates the adsorbed active oxygen atom (O*) as a transient species. In order to overcome the OER, the design of catalysts with a high Gibbs free energy for water oxidation but with a low one for CH_4 activation is highly required, and V_2O_5, TiO_2, SnO_2, PtO_2, and RhO_2 meet the conditions well. Theoretically, the operation in potentials close to 1.23 V_{NHE} is amenable to suppress the OER. The emergence of high-valent metal oxidation states and the change in the surface free energy would increase the coverage of active M–O sites and modify the reaction pathway. Regarding TiO_2/RuO_2 composites, the introduction of V_2O_5 switches the reaction pathway as follows.[40] Two ruthenium redox couples, $Ru^{4+/6+}$ and $Ru^{3/+4+}$, in RuO_2 participate in the production of oxygenates and affect the selectivity of the final products. For the formation of methanol, Ru^{6+} is reduced to Ru^{4+} sequentially following (i) $CH_4 + RuO_2^{2+} \rightarrow CH_3{-}RuO_2^+ + H^+$ and (ii) $CH_3{-}RuO_2^+ + H^+ \rightarrow CH_3OH + RuO^{2+}$. On the other hand, formaldehyde is formed by the conversion of ruthenium ($Ru^{6+} \rightarrow Ru^{4+} \rightarrow Ru^{3+}$) following the reactions $CH_4 + 2RuO_2^{2+} \rightarrow RuO^+{-}O{-}CH_2{-}O{-}RuO^+ \rightarrow HCOOH + 2RuO^+$. However, in the presence of V_2O_5 on RuO_2, the redox couple of vanadium ($V^{5+/4+}$) may not donate enough electrons to form a double bond for formaldehyde and formic acid; thus, the selectivity toward methanol increases ($CH_4 + V_2O_4^{2+} \rightarrow CH_3{-}V_2O_4^+ + H^+$; $CH_3{-}V_2O_4^+ + H^+ \rightarrow CH_3OH + V_2O_3^{2+}$). Transition metal ions also can be utilized as a redox couple in a homogenous system, where metal centers of organometallic complexes dissolved in the electrolyte turn into a high-valent state by applying anodic bias. As shown in Fig. 5b, the Pt^{II} of chloroplatinate accepts CH_4 by electrophilic addition reaction, and deprotonation produces the $Pt^{II}{-}CH_3$ complex, which is further oxidized into the $Pt^{IV}{-}CH_3$ complex by virtue of the oxidation by the electrochemically-formed $[Pt^{IV}Cl_6]^{2-}$ (*i.e.*, the Shilov cycle catalyzed by the redox cycle of $[Pt^{IV}Cl_6]^{2-}$ and $[Pt^{II}Cl_6]^{2-}$).[41] When H_2O or HCl exists, the $Pt^{IV}{-}CH_3$ complex leads to the formation of methanol or methyl chloride, respectively. The mechanistic pathway based on the PEC oxidation of CH_4 is quite analogous to the electrochemical system. The surface-bound $^{\bullet}OH$ on the (010) facet of the WO_3 photoanode can oxidize *in situ* formed methanol, resulting in the selective formation of ethylene glycol (Fig. 5c).[42] A wide range of strategies to improve the active site and the activation of CH_4 toward the production of desired products will be discussed in the following section.

3. Selective oxidation of methane into oxygenates *via* light- and electricity-driven processes over heterogeneous catalysts

3.1. Photocatalytic CH_4 conversion

Photocatalysis is a tool to utilize photonic energy as a driving force for photocatalytic ($\Delta G^\circ < 0$: downhill process) and photosynthetic ($\Delta G^\circ > 0$: uphill process) reactions.[43] As mentioned before, the oxidation of CH_4 is a downhill process; thus, the Gibbs free energy for partial oxidation to obtain oxygenates is more unfavorable than that for the complete oxidation to CO_2 (*e.g.*, $\Delta G^\circ(CH_3OH) = -115$ kJ mol^{-1}; $\Delta G^\circ(CH_2OH) = -296$ kJ mol^{-1}; $\Delta G^\circ(CO_2) = -818$ kJ mol^{-1}).

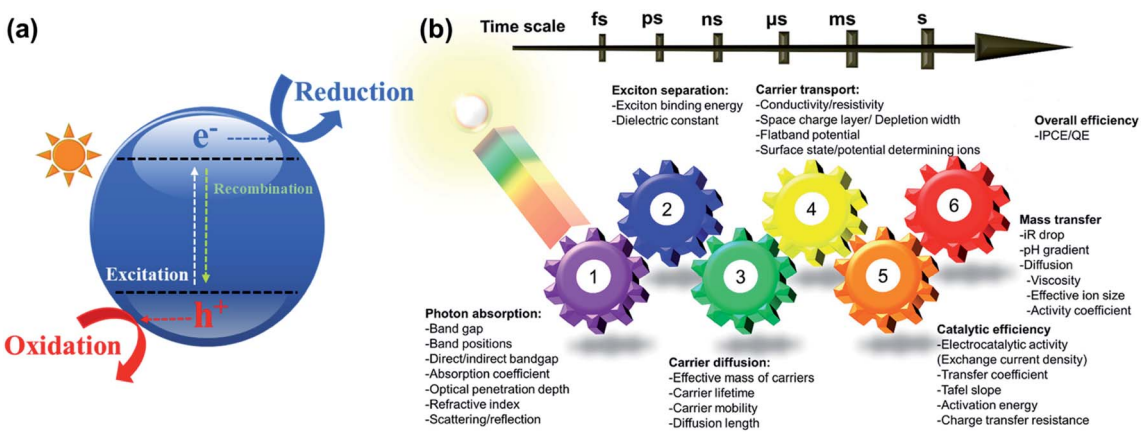

Fig. 6 (a) Simplified photocatalytic process. (b) Diverse factors influencing the photocatalytic performance. IPCE and QE refer to 'incident-photon-to-electron conversion efficiency' and 'quantum efficiency', respectively. Reproduced with permission.[44] Copyright 2017, American Chemical Society.

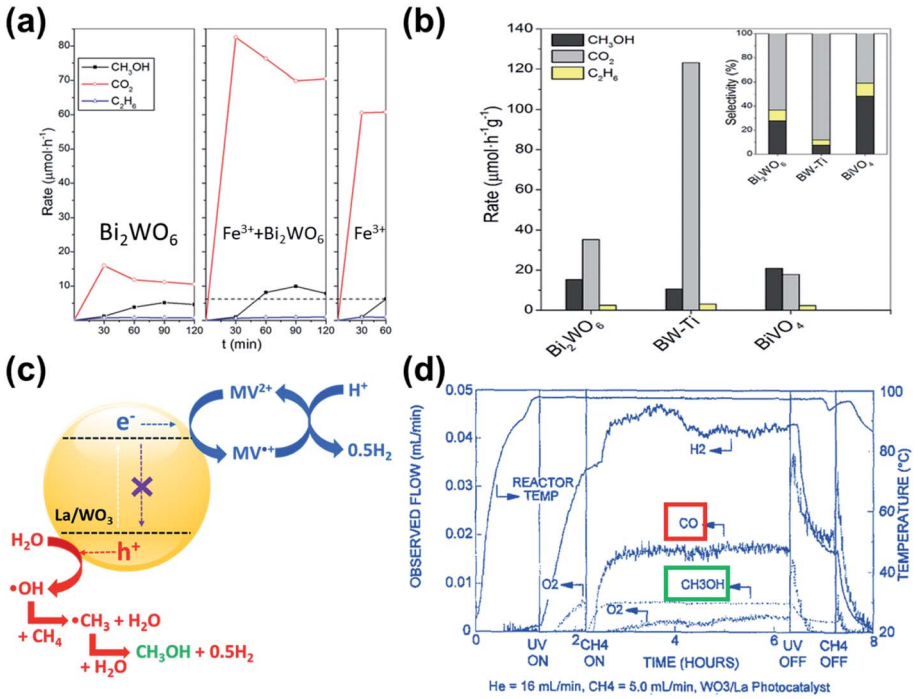

Fig. 7 (a) Photocatalytic oxidation of CH_4 using Bi_2WO_6, Bi_2WO_6 with Fe^{3+} (1 mM), and a solution of Fe^{3+}. (b) Different coversion rate and selectivity of CH_3OH, CO_2, and C_2H_6 for Bi_2WO_6, Bi_2WO_6/TiO_2, and $BiVO_4$ photocatalysts. Reproduced with permission.[29] Copyright 2014, American Chemical Society. (c) Proposed mechanism mediated $MV^{2+/\bullet+}$ for the partial oxidation of CH_4 in La-doped WO_3. (d) Time-dependent profile of products including CH_3OH, CO, H_2, and O_2 under dark and light irradiation for La-doped WO_3. Reproduced with permission.[27] Copyright 1997, Elsevier.

Although the schematic diagram representing the generation of electron–hole pairs and the interfacial charge transfer is simply depicted (Fig. 6a), understanding the detailed photophysical and photochemical processes is very difficult. Indeed, various factors should be considered to design highly active photocatalysts (Fig. 6b). Takanabe articulates the mechanistic pathway of photogenerated electron–hole pairs with considering time scale in his review article.[44] The photocatalytic performance is governed by (i) photon absorption, (ii) exciton separation, (iii) carrier diffusion, (iv) carrier transport, (v) catalytic efficiency, and (vi) mass transfer of reactants and products. The excitation of the electron from the valence band to the conduction band (*cf.*, from HOMO to LUMO in homogeneous photocatalysts) and the relaxation of the electron and hole to the band edge level occur in femtoseconds and in the range of femto to picosecond time scale, respectively.[45] Free charge carriers separated from excitons in nano to microseconds are delivered to the surface, which participate in the redox reaction within milliseconds to seconds. Therefore, the optimization of the electronic structure of the photocatalyst can improve the photon absorption, exciton separation, carrier diffusion, and carrier transport, which is a descriptor of how efficiently generation and transfer of the charge carriers to the surface take places. In particular, the introduction of catalytically active sites on the surface of photocatalysts such as defect sites, functional groups, and cocatalysts would help to facilitate C–H activation in terms of the dehydrogenation and deprotonation of CH_4. The control of the materials' morphologies and the design of reactors can solve the mass transfer problems of CH_4 and gas phase products.

Some factors influencing the redox reaction such as experimental conditions, nature of the oxidants, sacrificial reagents, morphology, and surface properties of the photocatalysts should be considered for the effective conversion of CH_4.[46,47] Photocatalytic partial oxidation of CH_4 can be achieved under relatively low temperature and pressure.[20,48] Contrarty to thermocatalysis, the mild experimental conditions make it the systematic build-up of reactors much more easy. On the other hand, the addition of oxidants including H_2O_2, nitric oxide (NO), and O_2 could accelerate the photocatalytic activation of CH_4 by means of the emergence of highly active radical species such as $^{\bullet}OH$ or $^{\bullet}O_2^-$.[49–51] The introduction of suitable sacrificial reagents can also boost up the reaction kinetics with scavenging either photogenerated electrons or holes. Accordingly, more charge carriers survived against the recombination possibly accelerate the activation of CH_4.[52] The dehydrogenation of CH_4 can be achieved by photogenerated holes directly, and the addition of electron acceptors such as Cu^{2+}, Ag^+, Fe^{3+}, and methyl viologen (MV^{2+}) may facilitate the kinetics since they are endowed with prolonged lifetime of holes.[20,22,53] The concept is analogous to a three-electrode system in electrochemical cells. Consistent with many other studies, the morphology and surface functionality of photocatalysts have significant impact on the photocatalytic oxidation of CH_4.[20,46]

A systematic investigation on the parameters influencing the partial oxidation of CH_4 to CH_3OH was conducted using

bismuth-based photocatalysts (*e.g.*, Bi_2WO_6, Bi_2WO_6/TiO_2, and $BiVO_4$).[29] The experiment conditions were as follows: medium-pressure mercury lamp (450 W), 55 °C, CH_4 : He (20 : 80) mixture with continuous purging (22.4 mL min^{-1}), and 1 g L^{-1} catalyst. Under catalyst-free conditions, the direct photolysis of water converted CH_4 into CH_3OH, CO_2, and C_2H_6. The selectivity for these products was 22.3, 59.7, and 18.1%, respectively. The CH_4 conversion and CH_3OH production rate was 0.8% and 2.1 μmol h^{-1}, respectively. The higher selectivity to CH_3OH (27.6%) and production rate (4.6 μmol h^{-1}) were achieved by the photocatalytic process with Bi_2WO_4, whereas the lower selectivity toward C_2H_6 (9.0%) was observed. When the temperature increased from 55 to 90 °C, the formation of C_2H_6 was markedly enhanced (almost 3-fold) with a negligible amount of CH_3OH. This could be ascribed by a high concentration of $^{\bullet}CH_3$ in terms of the dehydrogenation of CH_4 by $^{\bullet}OH$ in the presence of an excess amount of water vapor. In order to check the effect of dissolved oxygen as an electron acceptor, O_2 was continuously purged. While the production of CO_2 sharply rose (almost 20-fold), the formation of C_2H_6 was almost negligible and the CH_3OH production rate was barely affected. Introducing Fe^{3+} as a more effective electron scavenger greatly accelerated the evolution of CO_2, which was probably due to the enhanced charge separation and the overoxidation of CH_4 by $^{\bullet}OH$ (Fig. 7a). Interestingly, the higher selectivity toward CH_3OH (below 10%) was obtained in spite of the sharp increase in the total conversion (~7%). The blank test with Fe^{3+} solution showed the oxidation of CH_4 to CH_3OH, CO_2, and C_2H_6, and was attributed to hydroxyl radicals produced in the photo-Fenton process under UV light irradiation. The fabrication of Bi_2WO_6/TiO_2 and $BiVO_4$ was carried out to investigate the effect of the ability of charge separation and the conduction band energy level on CH_4 oxidation, respectively (Fig. 7b). Among the three samples, Bi_2WO_6/TiO_2 showed the highest CO_2 production rate and lowest CH_3OH production rate, which might be due to the production of more $^{\bullet}OH$. Despite such a low CH_4 conversion, the selectivity (*i.e.*, higher CH_3OH, lower CO_2, and C_2H_6 production) makes $BiVO_4$ a promising material.

Noceti *et al.* synthesized La- and Pt-doped WO_3 and carried out the photocatalytic activity test in the presence of MV^{2+} as an electron acceptor. This allowed photogenerated holes to oxidize H_2O to $^{\bullet}OH$ effectively instead of the recombination with electrons (Fig. 7c).[27] $^{\bullet}OH$ induced the dehydrogenation of CH_4 to $^{\bullet}CH_3$, and CH_3OH was generated by the reaction between $^{\bullet}CH_3$ and water (or $^{\bullet}OH$). The electron transfer from the conduction band to protons mediated by $MV^{2+/\bullet+}$ led to the production of H_2. The La-doped WO_3 showed a relatively good catalytic activity (*cf.*, about 4% of CH_4 conversion) under mild conditions (at 94 °C and under a constant gas flow of CH_4), where by-products including CO, H_2, and O_2 appeared (Fig. 7d). In the presence of H_2O_2 as a source to make $^{\bullet}OH$, the loading of FeOOH on WO_3 significantly improved the photocatalytic conversion of CH_4. However, an excess amount of H_2O_2 significantly reduced the production of the desired products (*i.e.*, a poor selectivity) owing to overoxidation.[54] The introduction of NO_2^- as an electron scavenger in the $BiVO_4$-dispersed solution lifted up the formation of $^{\bullet}OH$ in terms of the concomitant water oxidation by holes. Consequently, the selectivity of CH_4 to CH_3OH reached up to 93.0% but the low conversion problem still remained.[55]

$BiVO_4$ with unique morphologies was also investigated for CH_4 conversion. Zhu *et al.* compared the photocatalytic activity of $BiVO_4$ with different morphologies, and concluded that the bipyramid $BiVO_4$ with (102) and (012) surface facets was favorable for the production of CH_3OH relative to the platelet-type one with (001) facets.[30] The selectivity toward CH_3OH reached up to 85% and the mass activity was recorded as 112–134 μmol

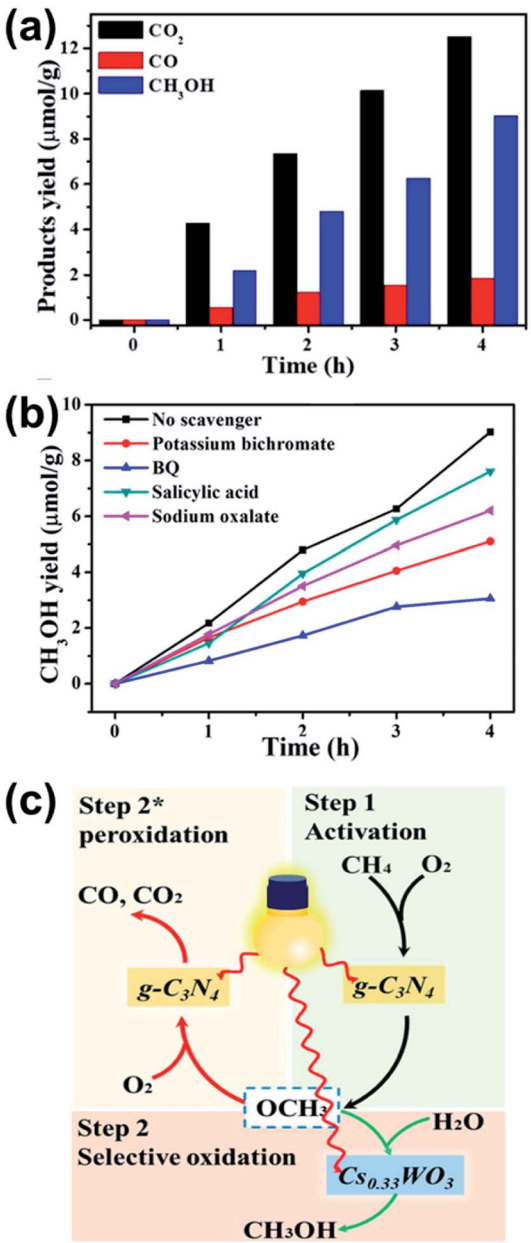

Fig. 8 (a) Time-dependent formation of CO_2, CO, and CH_3OH for g-C_3N_4@$Cs_{0.33}WO_3$ sample under irradiation. (b) Trapping of the radical species; herein, $K_2Cr_2O_7$, *para*-quinone, salicylic acid, and $Na_2C_2O_4$ were used as sacrificial reagents for electrons, $O_2^{\bullet-}$, $^{\bullet}OH$, and holes, respectively. (c) Proposed mechanism for the conversion of CH_4. Reproduced with permission.[59] Copyright 2019, American Chemical Society.

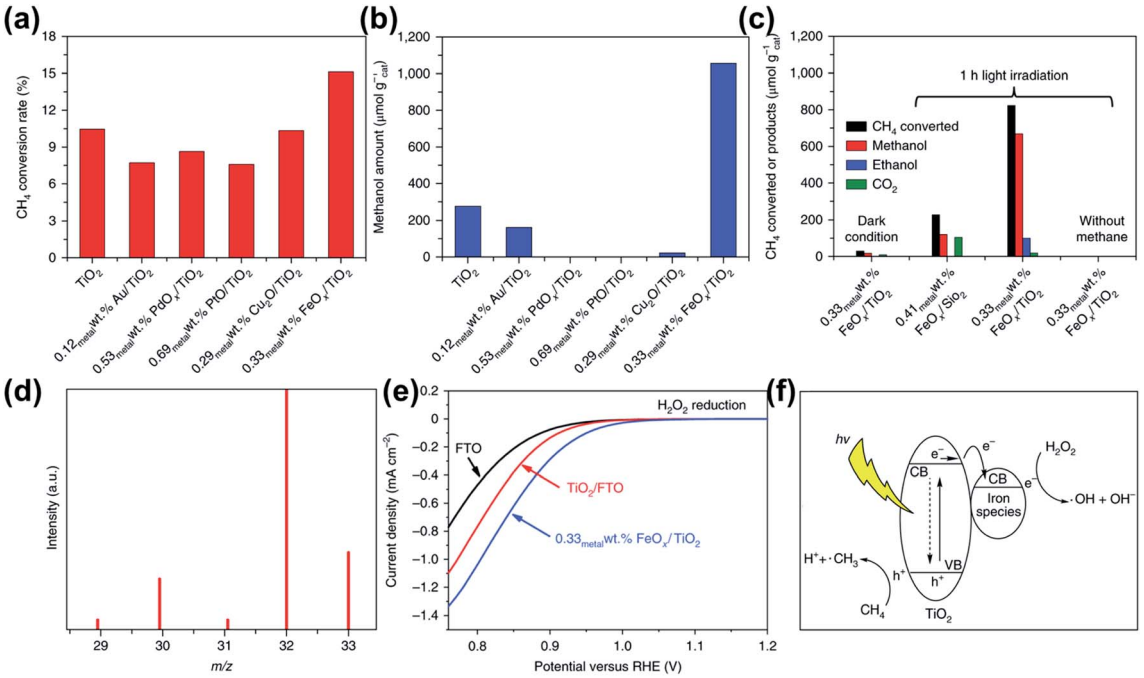

Fig. 9 (a) Photocatalytic conversion of CH_4 and (b) production of CH_3OH for metals or metal oxides loaded on TiO_2 after 3 h of full arc irradiation. (c) CH_4 conversion and product yield in control experiment. (d) Labelling experiment of liquid products using $^{13}CH_4$. (e) Comparison of LSV curves for FTO, TiO_2, and FeO_x/TiO_2. (f) Proposed reaction pathway on the production of radical species. Reproduced with permission.[60] Copyright 2018 Springer Nature.

h^{-1} g^{-1}. The high selectivity is probably originated from not only the effective interfacial hole transfer but also the adjusted surface energy for the activation of the C–H bond.

Carbon nitride (C_3N_4), consisting of only carbon and nitrogen, is one of cost-effective visible light-active photocatalysts, and its preparation is also quite easy.[56–58] Li *et al.* observed that CO and CO_2 were the main products when bare g-C_3N_4 was utilized, indicating that the overoxidation of CH_4 was severe.[59] However, it could be overcome by the fabrication of mace-like g–C_3N_4–decorated $Cs_{0.33}WO_3$ (g-C_3N_4@$Cs_{0.33}WO_3$) nanocomposites. As seen in Fig. 8a, the selectivity of CH_4 (1000 ppm) to CH_3OH, CO, and CO_2 was estimated to be 51.59%, 12.08%, and 36.33%, respectively, where the concentration of CH_3OH increased linearly with the irradiation time. $Cs_{0.33}WO_3$ was likely to protect the overoxidation of CH_3OH. According to the screening test result (Fig. 8b), it was concluded that both $^{\bullet}O_2^-$ and e^- are a main source to activate CH_4 (*i.e.*, the C–H bond activation *via* the reductive pathway mediated by $^{\bullet}O_2^-$) (Fig. 8c), which is in contrast to the result of other studies. The *in situ* EPR measurement should be helpful to determine the ROS mainly involved as well as to monitor the structure change of the catalysts during the reaction.

In the presence of H_2O_2, the selective conversion of CH_4 to CH_3OH was accomplished by virtue of the fabrication of highly dispersed iron species on TiO_2 photocatalysts.[60] In pristine TiO_2, CH_4 conversion and its selectivity toward CH_3OH during 3 h irradiation was 10.9% and 36%, respectively. As seen in Fig. 9a and b, the loading of noble metals on TiO_2 adversely affected the photocatalytic performance because zerovalent metals are known as a catalyst for the oxidation of CH_4 to CO and CO_2. Notably, the loading of 0.33 wt% iron species on TiO_2 enhanced the CH_4 conversion and the selectivity toward CH_3OH. By counting the formation of C_2H_5OH as the by-product, the total conversion to alcohols was estimated to be 97%. The control experiment clearly supports that the conversion of CH_4 mainly proceeded by the photocatalytic activation of H_2O_2 (Fig. 9c). Indeed, the labelling experiment using $^{13}CH_4$ revealed a new peak at $m/z = 33$, which indicates the formation of $^{13}CH_3OH^+$ from the photocatalytic process (Fig. 9d). Considering the X-ray absorption spectroscopy data, it was confirmed that FeO_x consisted of FeOOH and Fe_2O_3, whose oxidation state was close to +3. Along with the enhanced electron transfer process from the TiO_2 conduction band to FeO_x, the effective activation of H_2O_2 through a concomitant electron transfer improved the photocatalytic performance (Fig. 9e). As a result, it was proposed that the reaction between $^{\bullet}CH_3$ and $^{\bullet}OH$ produced CH_3OH; the formation of $O_2^{\bullet-}$ should be prohibited to avoid the overoxidation of CH_3OH to CO_2 (Fig. 9f).

ZnO is an UV light active photocatalyst, whose bandgap size is almost identical to TiO_2 (about 3.2 eV).[61] Without adding oxidants or cocatalysts, the photocatalytic conversion of CH_4 was almost negligible, indicating that the proper modification of ZnO is highly required.[50,62] The loading of cocatalysts (*e.g.*, Pt, Pd, Au, or Ag) on ZnO showed the good photocatalytic conversion of CH_4 to CH_3OH and CH_3OOH under aerobic conditions.[62] For instance, 0.1 wt% Au/ZnO resulted in a high photocatalytic activity of 125 μmol h^{-1} for oxygenates with selectivity over 95%. The isotope experiment exhibited that the

oxygen in CH_3OH and CH_3OOH stemmed from dissolved O_2 in water. The result supports the proposed mechanism that $^{\bullet}CH_3$ formed by the dehydrogenation of CH_4 with holes and $^{\bullet}OOH$ generated by the oxygen reduction with electrons are combined together and then turned into CH_3OH and CH_3OOH. It should be noted that water oxidation was not considered in the overall reaction. Therefore, the balance between the reductive and oxidative pathway is critical to increase the selectivity. The different mechanism was also proposed in the Au/ZnO photocatalyst.[50] The dehydrogenation of CH_4 to $^{\bullet}CH_3$ by $^{\bullet}OH$ can proceeded through both reductive and oxidative pathways; consequently, the reaction of $^{\bullet}CH_3$ with either $^{\bullet}OH$ or $O_2^{\bullet-}$ produced CH_3OH. In here, both H_2O and O_2 were invloved in the reaction.

3.2. Electrocatalytic CH_4 conversion

The electrocatalytic activation of CH_4 is able to be driven by either active oxygen on the surface electrode directly or free radicals formed at the electrode/electrolyte interface indirectly. In general, the cell performance is governed by the overpotential, surroundings, and the collision frequency, which are closely related to the activation energy, the ease of forming an active surface oxygen, and mass transfer of CH_4 and products, respectively.[63] In order to optimize the partial oxidation of CH_4 to the desired products, efforts on catalyst discovery, electrolyte engineering, and reactor design should be made considering the three factors shown in Fig. 10. To date, not only diverse electrocatalysts but also the engineering of electrolytes and reactors have been investigated for the partial oxidation of CH_4. The electrochemical system can be classified as (i) heterogeneous and homogeneous reaction, (ii) high and low temperature process, (iii) cathodic and anodic reaction, (iv) solid oxide and liquid electrolyte, and (v) fuel cell and electrolyzer type cell. In previous review articles, the effects of electrocatalysts, reaction conditions, and cell configurations on the formation of final products have already been well discussed and summarized in tables.[20,26,63–73] In this review, we mainly focused on the theoretical approach to interpret the CH_4 partial oxidation process on active sites in mild conditions, and overviewed the recent research results.

Transition metal oxides.[74] The electrocatalytic oxidation of CH_4 on transition metal oxides proceeds through the physical adsorption of CH_4, followed by the activation of the C–H bond. Fig. 11a shows the products obtained from the oxidation of CH_4 over various transition metal oxide catalysts. CO_2 evolution was only observed both for TiO_2, IrO_2, and PbO_2 in phosphate buffer and for PtO_2 in KCl electrolyte. The inactivity of PtO_2 in phosphate buffer was due to the poisoning of Pt covered by phosphate ions. The physical adsorption of CH_4 transformed the tetrahedral symmetry of CH_4 to the distorted structure (D_{2d}) with the H–C–H bond angle of about 120°, which scaled with the electrostatic interaction between CH_4 and transition metal oxides. Therefore, the experimentally measured CH_4 binding energy linearly increased with the Madelung potential of the metal in transition metal oxides (Fig. 11b). TiO_2, IrO_2, PbO_2, and PtO_2, classified as active catalysts, have a higher CH_4 binding energy (>0.23 V) and a lower Madelung potential (<−40 V). The inactivity of ZrO_2 and SnO_2, despite satisfying the condition, was ascribed to the poor electrical conductivity and a small number of active sites, respectively. The introduction of Cu_2O_3 on TiO_2 resulted in 6% faradaic efficiency at 0.35 mA cm^{-2} current density for the production of CH_3OH, in which *OH was provided from Cu to $*CH_3$-populated TiO_2. Cu has a lower energy barrier for the reaction of $*CH_3$ with *OH and is resistant to the overoxidation of CH_3OH (Fig. 11c). The DFT-predicted reaction profile for OER is depicted for the fully reduced state (Fig. 11d) and fully oxidized one (Fig. 11e) according to the reaction pathway ($*H_2O \rightarrow *OH + 0.5H_2$; $*OH \rightarrow *O + 0.5H_2$; $O^* + H_2O \rightarrow * + O_2 + H_2$). OER was favorable for the undercoordinated metal sites of SnO_2, TiO_2, and IrO_2 but on the

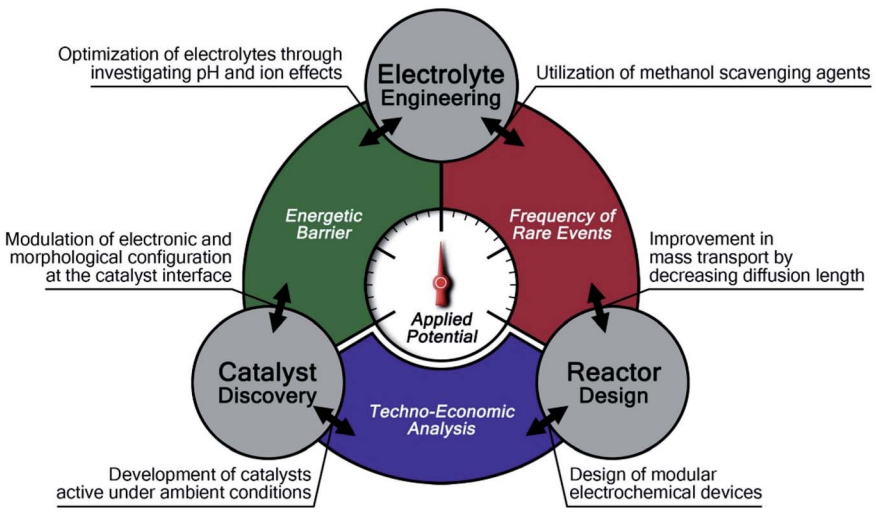

Fig. 10 Parameters consisting of catalyst discovery, electrolyte engineering, and reactor design interconnected with three factors including energetic barrier, frequency of rare events, and techno-economic analysis to be considered for the development of effective electrocatalytic CH_4 partial oxidation systems. Reproduced with permission.[63] Copyright 2019, Elsevier.

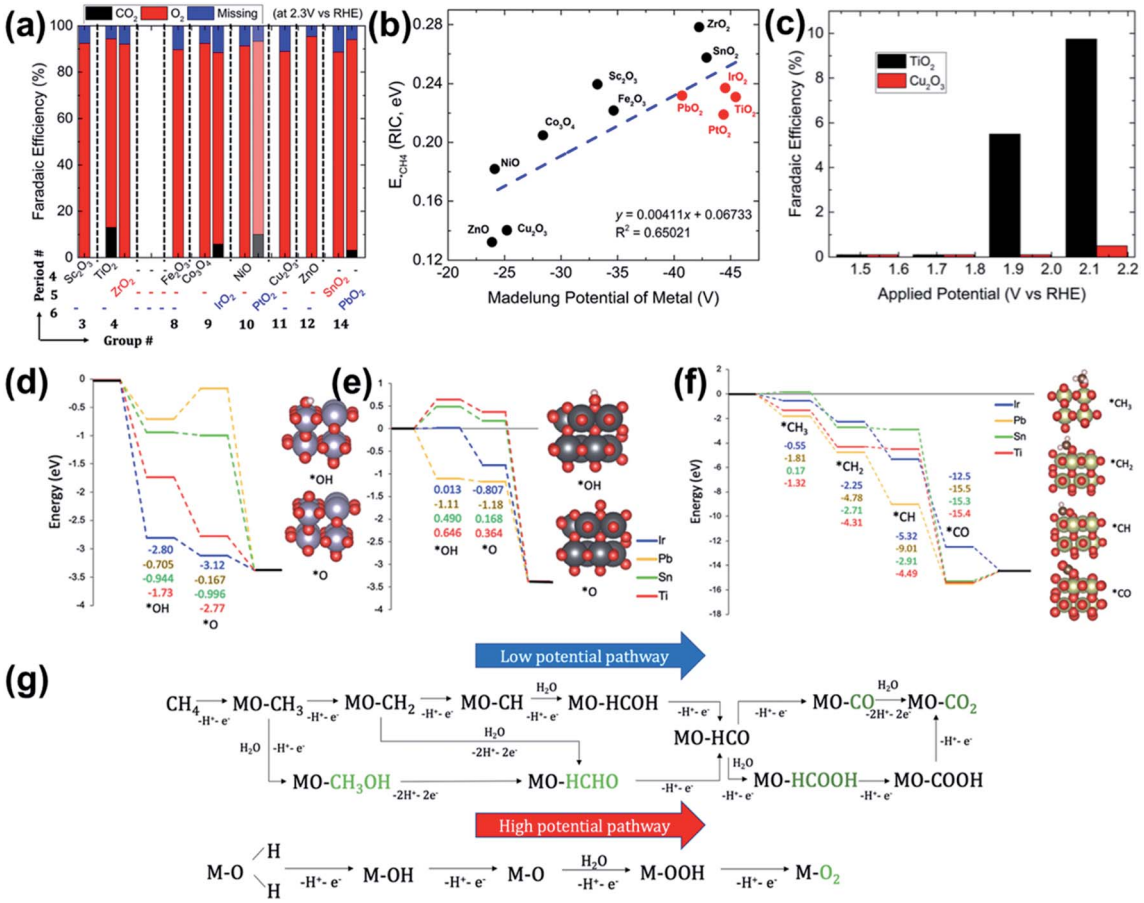

Fig. 11 (a) CH_4 oxidation products and faradaic efficiency over diverse transition metal oxides in 0.1 M potassium phosphate buffer (pH = 7). The result of PtO_2 was obtained in 1 M KCl (pH = 7) because of inactivity in 0.1 M potassium phosphate buffer. (b) Scaling relationship between the measured binding energy of $*CH_4$ and the Madelung potential of metal in transition metal oxides. (c) Faradaic efficiency of methanol oxidation to CO_2 over TiO_2 with applied potential in the presence/absence of Cu_2O_3. Reaction profile (d) for OER on the undercoordinated metal sites, (e) for OER on the bridging oxygen binding site, and (f) for CH_4 oxidation on the undercoordinated metal sites in transition metal oxides. (g) Possible reaction pathways for CH_4 oxidation and OER in an aqueous electrolyte. Reproduced with permission.[74] Copyright 2021, National Academy of Sciences.

bridging O site of PbO_2. Fig. 11f shows the reaction profile for CH_4 oxidation following five steps (1st: $* + CH_4 \rightarrow *CH_3 + 0.5H_2$; 2nd: $*CH_3 \rightarrow *CH_2 + 0.5H_2$; 3rd: $CH_2* \rightarrow *CH + 0.5H_2$; 4th: $*CH + H_2O \rightarrow *CO + 1.5H_2$; 5th: $*CO + H_2O \rightarrow * + CO_2 + H_2$). The C–H bond activation was energetically advantageous for TiO_2, IrO_2, and PbO_2; however, SnO_2, with a lower M–O site, encountered a higher energy barrier. According to reactant-impulse chronoamperometry (RIC) and open circuit potential (OCP) changes along with DFT calculation, the reaction mechanism proposed that CH_4 oxidation proceeded through the formation of $*CH_x$ and $*CH_xO_y$ intermediates at lower and higher potentials, respectively (Fig. 11g).

2D transition metal carbides (MXenes).[75] The DFT calculation of the electrocatalytic CH_4 oxidation on various 2D carbides (MXenes) offers important clues to understand the relation among the stability of active oxygen, the reactivity of C–H bond activation, and the selectivity toward specific oxygenates. Under applied anodic potential, the O-terminated surface was predominant rather than both metal-terminated and OH-terminated surface. The C–H bond was activated by an active oxygen (O*) derived from water oxidation (*i.e.*, hydroxyl adsorption: $H_2O + * \rightarrow OH* + H^+ + e^-$; deprotonation: $OH* \rightarrow O* + H^+ + e^-$). As the lower limit of electrochemical potential to form active oxygen (U_{form}, derived from $_{max}[\Delta G_{O*} - \Delta G_{O*}]/e^-$) is lower than the dissociation potential of active oxygen (U_{diss}, calculated by $(\Delta G_{OOH*} - \Delta G_{O*})/e^-$), O* can be accumulated on the surface of the catalysts. As shown in Fig. 12a, the OER follows a volcano curve; thus, the MXenes at the right and left side of the volcano curve are suitable for CH_4 oxidation and OER, respectively. The change in C–H bond activation ($\Delta E_{a,TS} = E_{a,TS} - E_{CH4*}$) for the affinity energy of proton ($\Delta E_{OH*} - \Delta E_{O*}$) indicates that MXenes with a high proton affinity tend to stimulate the activation of the C–H bond (Fig. 12b). A Sabatier-like relation was observed between the stability of active oxygen and the reactivity of C–H bond activation. The active oxygen in Hf_2CO_2 and Zr_2CO_2 is too active but the stabilized O* in Ta_2CO_2, NbC_2O_2, and V_2CO_2 is too inert, consequently lowering the CH_4 conversion yield. Contrary to MXenes composed of single

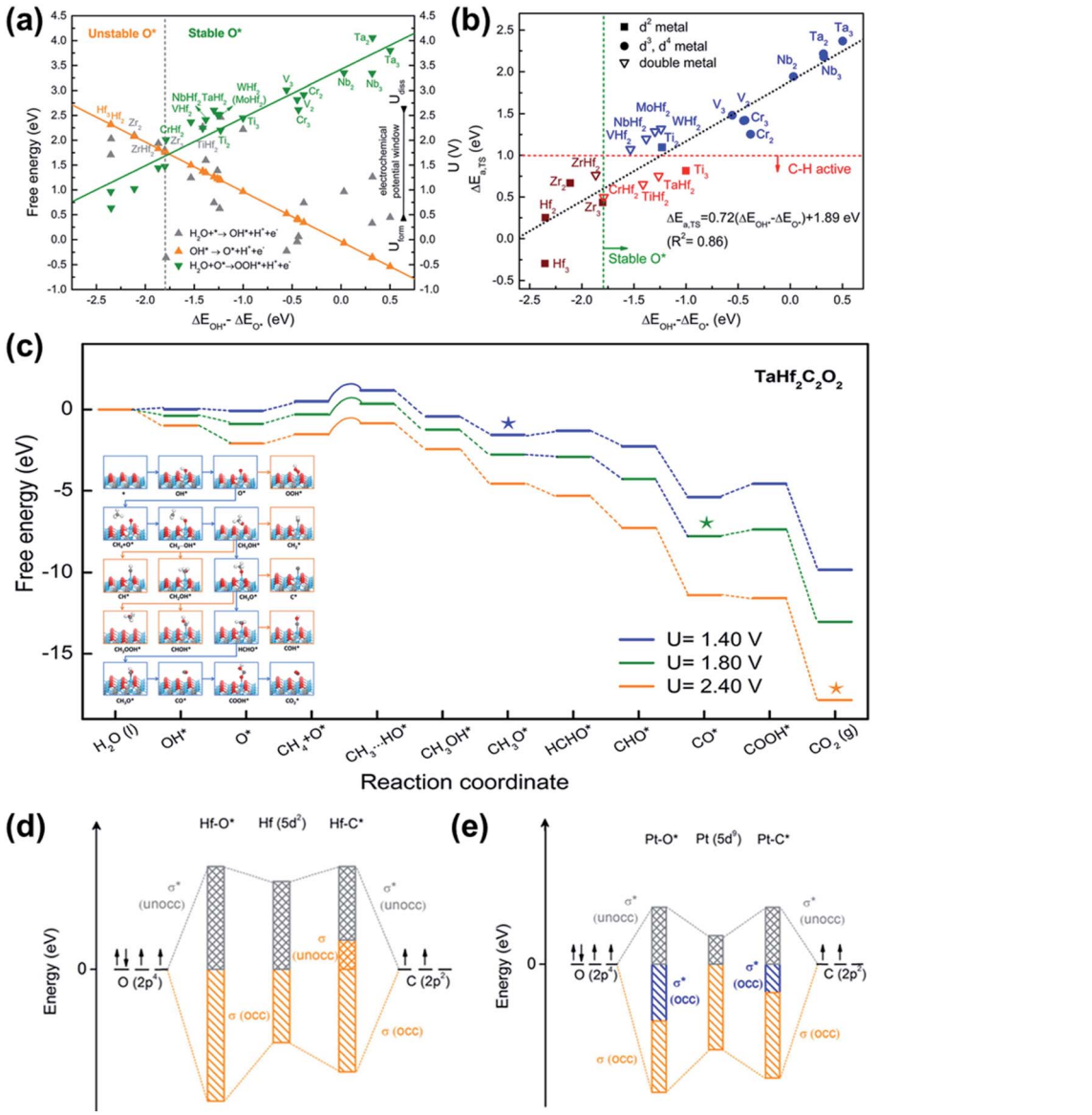

Fig. 12 (a) Free energies of the OH*, O*, and OOH* formation steps in OER as functions of $\Delta E_{OH*} - \Delta E_{O*}$. (b) The energy barrier of C–H bond activation ($\Delta E_{a,TS}$; TS means transition state) as a function of $\Delta E_{OH*} - \Delta E_{O*}$. (c) Free energy diagram of stable products in methane oxidation at different electrode potentials (1.40, 1.80, and 2.40 V_{RHE}). Inset: schematic diagram of the electrocatalytic conversion of CH_4 on $TaHf_2C_2O_2$ and blue arrows mean the energetically favorable route. Band filling of oxygen and carbon adsorbed on (d) $TaHf_2C_2O_2$ and (e) metal Pt. Reproduced with permission.[75] Copyright 2021, Elsevier.

metals, $CrHf_2CO_2$ and $TaHfCO_2$ are energetically favorable for CH_4 activation. Depending on the applied potential for $TaHfC_2O_2$, the formation of intermediates, known as relatively stable species, was changed (*i.e.*, CH_3O*, CO*, and CO_2* at 1.4, 1.8, and 2.4 V, respectively) (Fig. 12c). On $TaHf_2C_2O_2$, the production of oxygenates was preferred to that of hydrocarbons (inset in Fig. 12c), which is supported by the calculation based on the projected density of states (PDOS) and projected crystal orbital Hamilton population (pCOHP). For the Hf ($5d^2$) with a few d electrons in $TaHf_2C_2O_2$, the Hf–O bond is stronger than the Hf–C bond; therefore, the formation of oxygenates is predominant (Fig. 12d). The observation that only hydrocarbons, CO, and CO_2 were produced on metallic Pt in a previous study[76] would be due to a strong interaction between Pt and C. The electrons in Pt–C that are able to occupy the anti-bonding orbital are fewer than those in Pt–O (Fig. 12e).

Only few research articles have reported the electrocatalytic partial oxidation of CH_4 at room temperature.[40,77–81] The introduction of V_2O_5 in TiO_2/RuO_2 composites increased the current density and selectivity toward CH_3OH when a gas diffusion electrode (GDE) cell was utilized in 0.1 M Na_2SO_4.[40] The redox couple of $V^{5+/4+}$ would not give electrons to form a double bond; thus, the selectivity toward CH_3OH increased against HCHO and HCOOH. Park's group reported the partial oxidation of CH_4 to oxygenates using Co_3O_4/ZrO_2 nanocomposites,[77] Co_3O_4-incorporated ZrO_2 nanotubes,[79] and $ZrO_2/NiCo_2O_4$ nanowires[81]

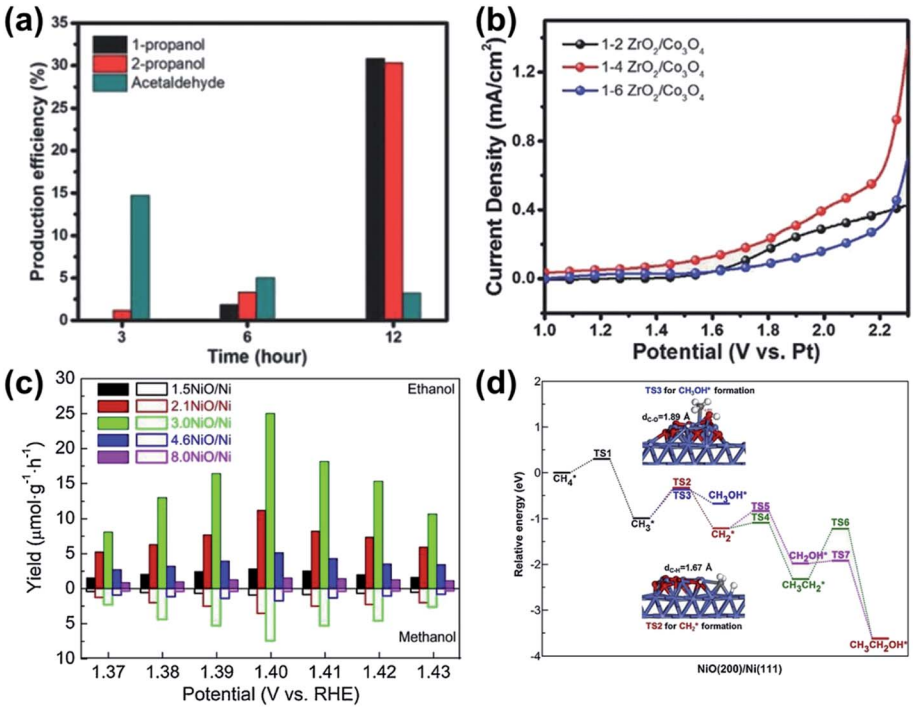

Fig. 13 (a) Production efficiencies of 1-propanol, 2-propanol, and acetaldehyde with the reaction time for ZrO_2/Co_3O_4. (b) LSV curves of ZrO_2/Co_3O_4 with a different amount of ZrO_2 loaded. Reproduced with permission.[77] Copyright 2017, Wiley. (c) Yields of ethanol and methanol produced over NiO/Ni catalysts with different NiO contents with increasing potential. (d) Energy profiles for CH_4 oxidation to CH_3OH and C_2H_5OH at the NiO(200)/Ni(111) interface. Reproduced with the permission.[78] Copyright 2020, Elsevier.

using the typical single cell reactor. The Co_3O_4/ZrO_2 nanocomposites led to the formation of acetaldehyde as a major intermediate in the first 3 h, and finally turned into 1- and 2-propanol as the main products after 12 h in 0.5 M Na_2CO_3 (Fig. 13a). It was proposed that the electrochemically formed carbonate radicals would initiate the dehydrogenation of CH_4

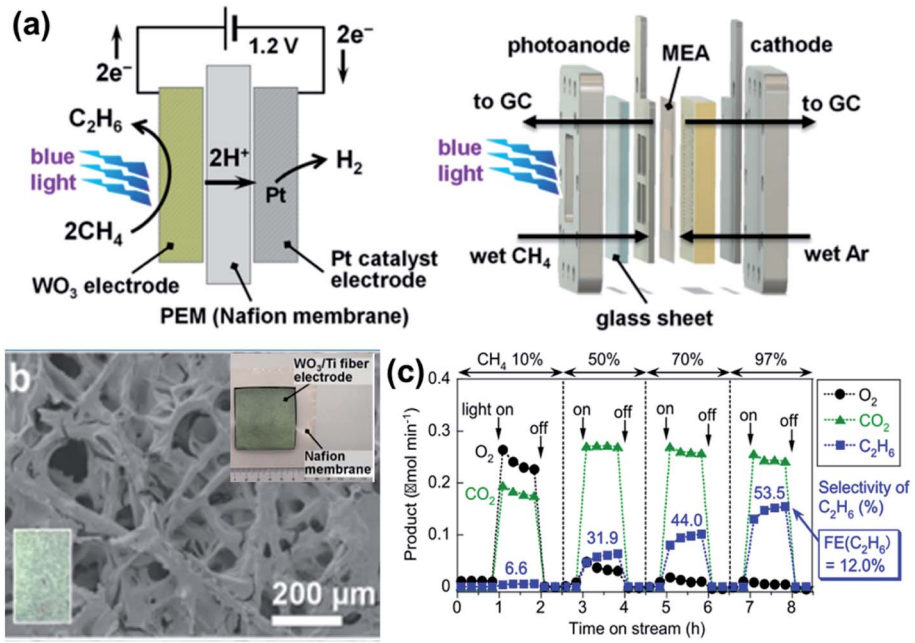

Fig. 14 (a) PEC system (left) and its expansion to MEA (right) for CH_4 activation. (b) SEM image of WO_3 deposited on Ti microfibers. Inset: picture of the PEC electrode (left lower) and MEA (right upper). (c) Time-dependent production of O_2, CO_2, and C_2H_6 in the photoanode compartment under 453 nm blue LED light irradiation at an applied voltage of 1.2 V. Reproduced with permission.[84] Copyright 2019, American Chemical Society.

and the addition reaction of $^{\bullet}CH_3$ to acetaldehyde generated C3 products. Herein, the role of ZrO_2 was assigned as a promoter to adsorb carbonates. In the control experiment, no increase in the LSV curve was observed for pristine Co_3O_4 regardless of CH_4 purging. With increasing ZrO_2 content, the current density increased and then decreased, supporting that the optimal ratio of ZrO_2 to Co_3O_4 should be considered to design highly-efficient electrocatalysts (Fig. 13b). The electrocatalytic performance was further enhanced either by the morphology control of Co_3O_4/ZrO_2 with Co_3O_4 nanoparticles embedded on the surface of ZrO_2 nanotubes[79] or ZrO_2/$NiCo_2O_4$ quasi-solid solution nanowires,[81] which improved the mass transfer problem of CH_4.

The electrocatalytic conversion of CH_4 to C_2H_5OH was investigated on NiO/Ni and Rh/ZnO catalysts. The NiO/Ni electrode in the potential range from 1.37 to 1.43 V_{RHE} produced C_2H_5OH, whose selectivity was recorded to be about 81–89% in 0.1 M NaOH.[78] Counting the formation of CH_3OH as a byproduct, the selectivity toward oxygenates was estimated to be over 90%. The yield of C_2H_5OH and CH_3OH increased up to 1.40 V, and then decreased with applied potential (Fig. 13c). The DFT calculation revealed that the formation of C_2H_5OH is more favorable than that of CH_3OH, and the proposed reaction pathway follows the sequential steps (*i.e.*, $CH_4^* \rightarrow CH_3^* + H^*$; $CH_3^* \rightarrow CH_2^* + H^*$; $CH_2^* + OH^* \rightarrow CH_2OH^*$; $CH_3^* + CH_2OH^* \rightarrow CH_3CH_2OH^*$) (Fig. 13d). Regarding Rh/ZnO nanosheets, the conversion, faradaic efficiency, and selectivity toward C_2H_5OH was measured as 789 μmol g_{cat}^{-1} h^{-1}, 22.5%, and 85%, respectively, at 2.2 V_{RHE} in 0.1 M KOH.[80] It was suggested that Rh nanoparticles on ZnO nanosheets accelerated the adsorption of CH_4 and the formation of active oxygen species. The operando analysis is a powerful tool to understand the real-time process involved in the activation and conversion of CH_4. Hahn *et al.* investigated the activation of CH_4 on the Pt catalyst at room temperature using attenuated total reflectance-surface enhanced infrared absorption spectroscopy (ATR-SEIRAS), and it was confirmed that the intermediates –CHO (aldehyde) and –COOH (acid) were formed during the oxidation of CH_4.[82] Furthermore, the intermediates were detected by *in situ* linear potential sweep-Fourier transform infrared spectroscopy (LPS-FTIRS). Together with CO_2 (2345 cm^{-1}), CO (2020 cm^{-1}), and H_2O (1650 cm^{-1}) peaks, a broad peak (1750 cm^{-1}) was observed due to the formation of aldehydic and ketonic species with the –CO moiety. At 1.46 V, the intermediate peaks for –CHO (1719 cm^{-1}) and –COOH (2027 cm^{-1}) were measured on the Pt electrode surface. The electrochemical oxidation of CH_4 over Pt/C, Pt/C-ATO, Pd/C, and Pd/C-ATO electrocatalysts was also confirmed by *in situ* ATR-Fourier transform infrared (ATR-FTIR) spectroscopy.[83] Herein, the intermediates –CHO and CO were

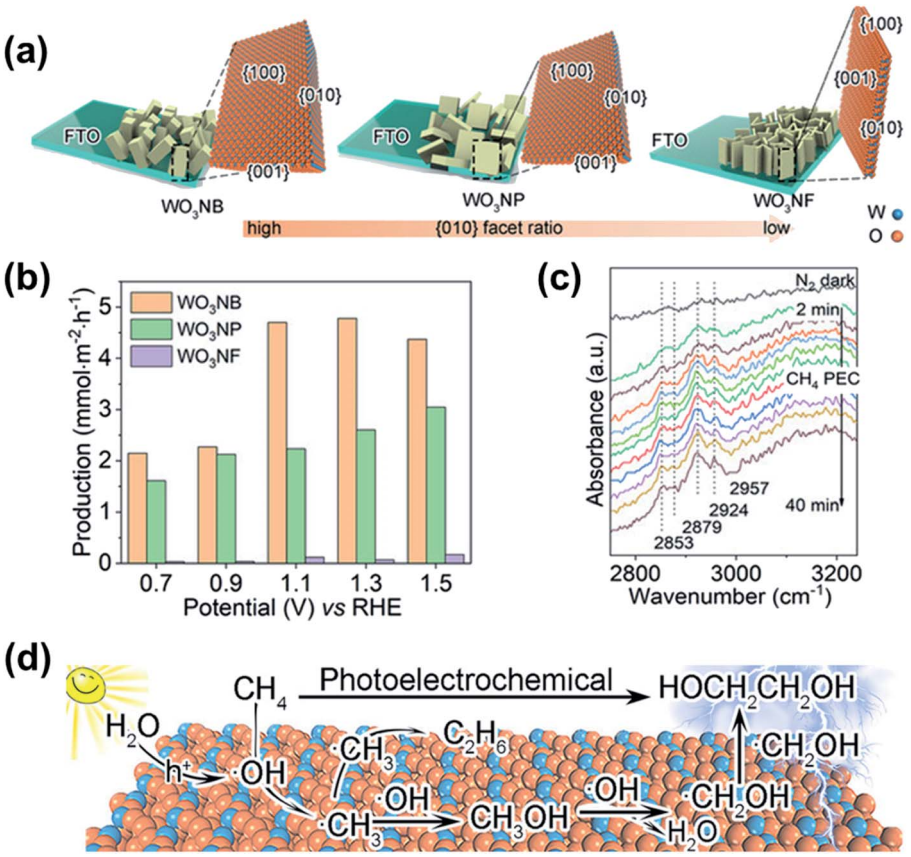

Fig. 15 (a) WO_3 with a different (010) facet ratio grown on FTO glasses. (b) EG production rate in term of PEC CH_4 conversion on WO_3 photoanodes under 100 mW cm^{-2} irradiation. (c) *In situ* DRIFTS for WO_3NB during the reaction. (d) Proposed mechanism for the conversion of CH_4 to EG. Reproduced with permission.[42] Copyright 2021, Wiley.

observed in the potential range from 0.05 to 1.2 V, which were clarified as intermediates for the production of CO_2.

3.3. Photoelectrochemical CH_4 conversion

When the Fermi level of the semiconductor and the chemical potential of the electrolyte (chemical species) are at equilibrium, 'band-bending' occurs depending on n-type and p-type materials. Under applied external bias or by the configuration of the tandem cell, photogenerated electron–hole pairs are separated, and the recombination is significantly retarded. In the n-type photoanode, the photogenerated holes transferred to the electrolyte/semiconductor interface initiate the oxidation. At the same time, the electrons collected on the counter electrode begin the reduction reaction. Ideally, the photogenerated holes oxidize CH_4 to oxygenates, while the electrons transferred to the cathode produce H_2. As mentioned before, ROS formed by water oxidation can attack and activate the stubborn C–H bond in terms of lowering the energy barrier, accompanying the dehydrogenation of CH_4 through a radical process. The technical advantages of the PEC cells including the controllable selectivity and production rate by applied potential, tunability of the electrode properties with the cocatalyst, and the facile fabrication of the cells are visible. However, it has failed to overcome a low efficiency and selectivity problem for the oxidation of CH_4. Due to limited studies, we discuss the PEC conversion of CH_4 to oxygenates and hydrocarbons as well.

Amano *et al.* reported the activation of CH_4 on WO_3 photoanode with a high quantum efficiency under visible light irradiation at room temperature.[84] Applying external bias enabled the use of photogenerated electrons for H_2 production and the deeper depletion layer formed in WO_3 suppressed the recombination of charge carriers. In order to solve the low solubility and mass transport problems of CH_4, a bimodal (meso and macro) porous WO_3 photoanode was fabricated *via* the deposition of WO_3 nanoparticles on the microporous 3D Ti microfiber. The concentration of protons between the photoanode and cathode chambers was balanced by the assembly with Nafion membrane (Fig. 14a and b). Since the valence band maximum of WO_3 is more positive than the standard electrode potential of CH_4 oxidation ($CH_4 + h^+ \rightarrow {}^{\bullet}CH_3 + H^+ + e^-$; $E^{\circ}({}^{\bullet}CH_3/CH_4) = 2.06\ V_{SHE}$), the photogenerated holes can dehydrogenate CH_4 into a methyl radical (${}^{\bullet}CH_3$). Consequently, the homogeneous coupling of ${}^{\bullet}CH_3$ brought about the production of C_2H_6 (${}^{\bullet}CH_3 + {}^{\bullet}CH_3 \rightarrow C_2H_6$). The gas–electrolyte–solid triple-phase boundary significantly improved the oxidation of the inert

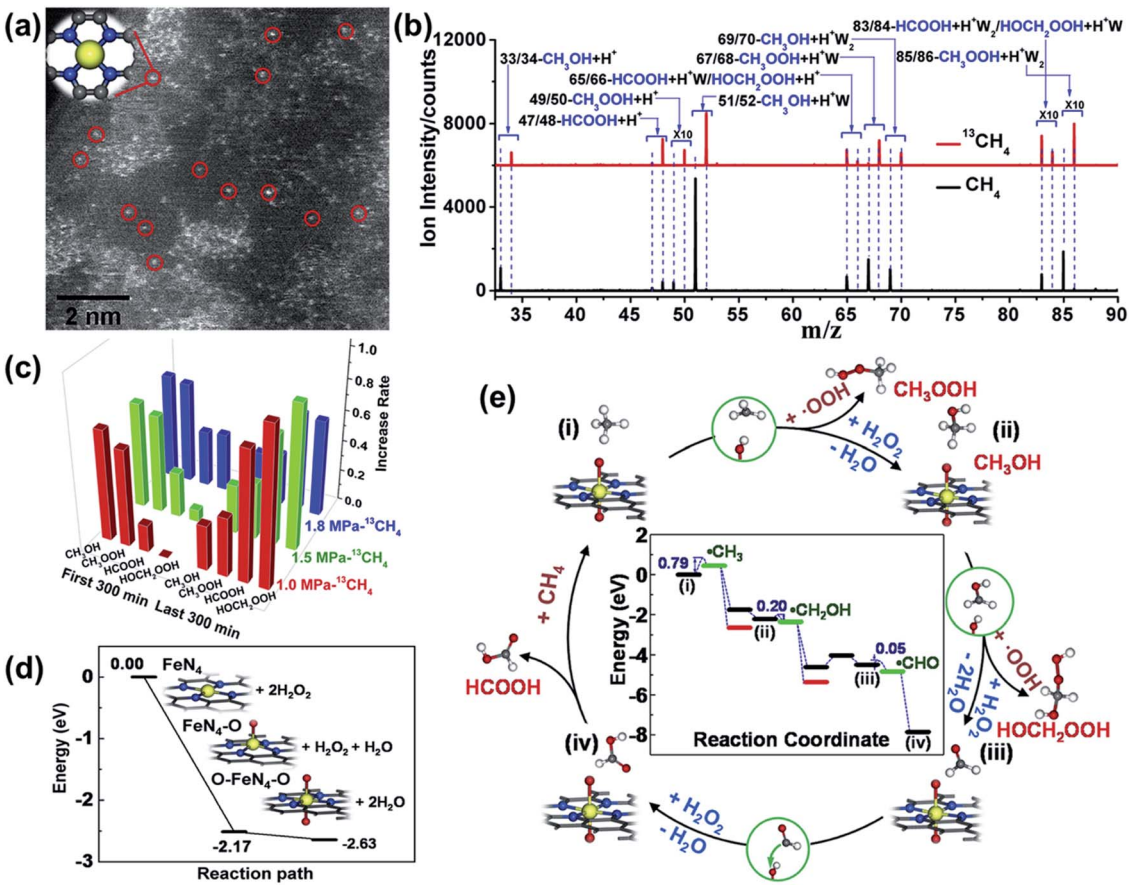

Fig. 16 (a) HAADF-STEM image of FeN_4/GN. Single iron atoms are marked by red circles. (b) TOF-MS data for the labelling experiment using $^{13}CH_4$. The W denotes water molecule. (c) *In operando* TOF-MS data collected under different pressure of $^{13}CH_4$. (d) Energy change of FeN_4 center by the adsorption of H_2O_2. (e) Proposed mechanism on the partial oxidation of CH_4 over FeN_4/GN catalysts. Reproduced with the permission.[92] Copyright 2018, Elsevier.

C–H bond of CH_4 and led to the formation of CO_2 and C_2H_6. When the concentration of CH_4 was reduced in the feed (*i.e.*, the stream of Ar with 10% CH_4 and 3 vol% H_2O), the production of C_2H_6 was negligible (Fig. 14c). In reverse, as the concentration of CH_4 fed increased, C_2H_6 production steadily increased. Under 97/3 vol% of CH_4/H_2O stream, the selectivity and the faradaic efficiency toward C_2H_6 reached up to 53.5% and 12%, respectively. These results indicate that the access of gaseous CH_4 to the surface of the WO_3 photoanode is important for preferential C–H bond activation by photogenerated holes. The selectivity toward C_2H_6 could be improved by making the surface of WO_3 hydrophobic for the effective adsorption of CH_4 instead of water.

Ma *et al.* optimized the reactivity of $^{\bullet}OH$ on WO_3 *via* facet tuning to produce ethylene glycol (EG) under mild conditions without adding any oxidants.[42] Three WO_3 photoanodes with different (010) facet ratios including WO_3 nanobar arrays (WO_3NB), WO_3 nanoplate arrays (WO_3NP), and WO_3 nanoflake arrays (WO_3NF) were fabricated for comparison (Fig. 15a). Among them, WO_3NB with a predominant (010) facet revealed a superior CH_4 conversion performance. To confirm the production of $^{\bullet}OH$ on the catalysts with different facets, electron paramagnetic resonance (EPR) spectroscopy was measured using 5,5-dimethyl-1-pyrroline-*N*-oxide (DMPO) as a spin-trapping agent. The signal for DMPO–$^{\bullet}OH$ on WO_3NB was stronger than that of other WO_3 structures. Based on the result that no H_2O_2 formation was observed during the experiment, it was expected that the oxidation of water was the only source to provide $^{\bullet}OH$. Consequently, the EG production rate, selectivity, and solar-to-fuel efficiency in WO_3NB were recorded to be 0.47 μmol cm^{-2} h^{-1}, 66%, and 0.12% at 1.3 V_{RHE}, respectively (Fig. 15b). The *in situ* diffuse reflectance infrared Fourier-transform spectroscopy (DRIFTS) data support that EG was steadily produced on the PEC cell (Fig. 15c). The typical peaks of EG at 2853 and 2924 cm^{-1} (*cf.*, assigned to methylene (CH_2) symmetric C–H stretching and antisymmetric C–H stretching, respectively) were measured, which increased with the irradiation time. Moreover, the emergence of methyl (CH_3) symmetric C–H stretching at 2879 cm^{-1} and antisymmetric C–H stretching of CH_3OH at 2957 cm^{-1} indicate that CH_3OH was formed as an intermediate during the PEC process. Therefore, the mechanism can be explained as follows: CH_3OH was formed by the

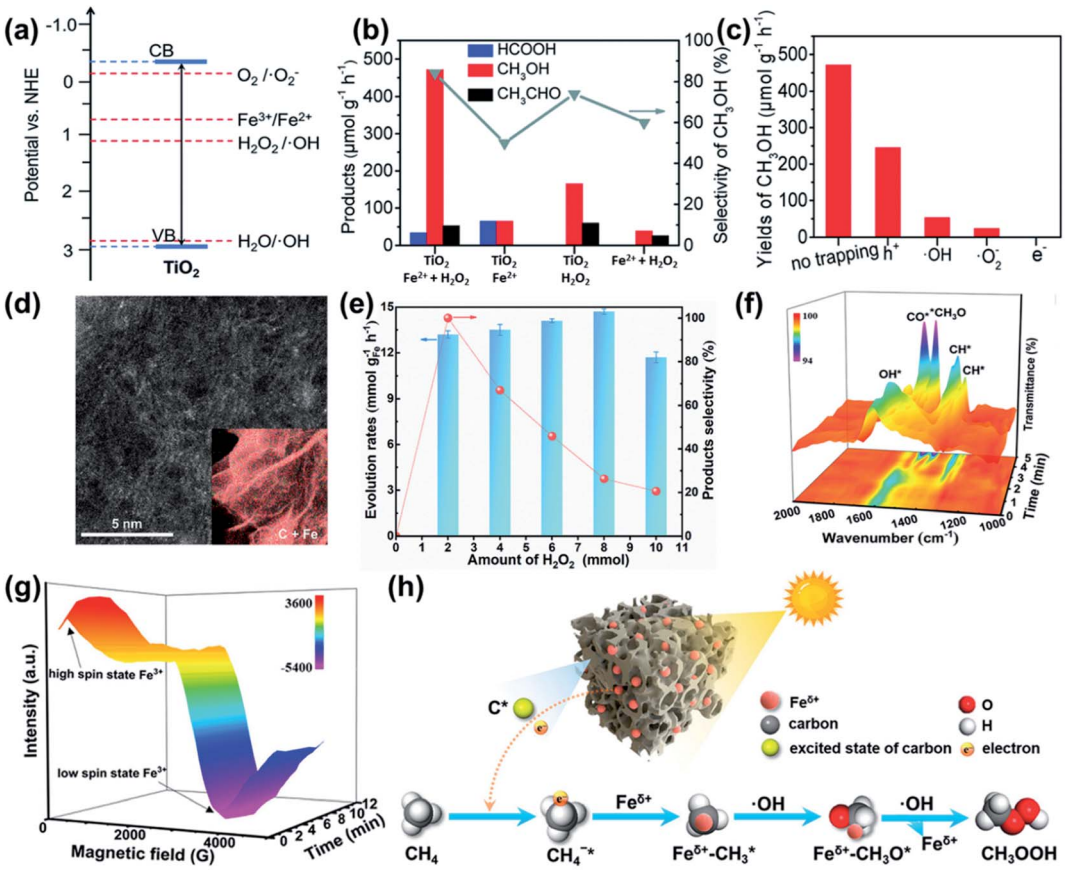

Fig. 17 (a) TiO_2 conduction and valence band position and redox potentials of the active species. (b) Yield of CH_4 to CH_3OH under AM 1.5 at room temperature for different systems. (c) Scavenger experiments of ROS (h^+, e^-, $^{\bullet}OH$, and $^{\bullet}O_2^-$). Reproduced with permission.[34] Copyright 2020, Royal Society of Chemistry. (d) HAADF-STEM image and elemental mapping of carbon and iron for 0.75FeCA800-4. (e) Photocatalytic conversion kinetics and selectivity for the partial oxidation of CH_4 to CH_3OOH, depending on the H_2O_2 concentration. (f) *In situ* DRIFTS spectra during photocatalysis. (g) *In situ* EPR spectra of the $Fe^{\delta+}$ contents with the irradiation time. (h) The proposed mechanism of the conversion of CH_4 to CH_3OOH over 0.75FeCA800-4. Reproduced with the permission.[106] Copyright 2021, American Chemical Society.

reaction between $^{\bullet}OH$ and $^{\bullet}CH_3$, which was further attacked by $^{\bullet}OH$, finally producing the EG (Fig. 15d).

It should be worth highlighting other metal oxide candidates for PEC cell applications. Fe_2O_3 (hematite) has a suitable valence band minimum for CH_4 oxidation and an ideal visible light absorption with n-type property, whose band gap energy was about 2.1–2.2 eV.[85,86] Iron oxide is abundant in nature, cheap, and non-toxic, and the hematite-based photoanode is very stable during OER in an alkali electrolyte.[87] $BiVO_4$ with a bandgap of 2.4 eV shows an excellent PEC OER performance and is relatively stable in neutral pH.[88,89] Metal chalcogenide, C_3N_4, and metal carbide are also good candidates for visible light PEC CH_4 oxidation because the outstanding photocatalytic activity was already reported for the partial oxidation of CH_4 in slurry-type systems.[90,91] The modification of the bulk and surface properties of semiconducting materials and cocatalysts or the introduction of highly active photocatalysts and electrocatalysts in PEC systems should be helpful to advance the design of the PEC device with high performance under sunlight.

3.4. Activation of oxidants for radical-assisted CH_4 conversion

While the direct interaction between the surface-active site of heterogeneous (photo)electrocatalysts and CH_4 stimulates the activation of CH_4 in terms of the dehydrogenation and deprotonation processes, free-standing radical species (especially, $^{\bullet}OH$ and $^{\bullet}Cl$) floating in the solution enable the extraction of hydrogen from CH_4. Like Shilov cycle (Fig. 5b), the supply of $^{\bullet}OH$ can be maintained by the Fenton process unless H_2O_2 is completely consumed. The ferric/ferrous redox cycle is regenerated by the electron transfer induced by photo and electrocatalysis. Under anaerobic conditions, a hole-mediated oxidation or an anodic reaction of water or chloride is the only way to produce active radical species. However, under aerobic conditions, the reductive pathway (*i.e.*, electron-mediated reactions) produces H_2O_2 and further electron transfer to *in situ* formed H_2O_2 generates $^{\bullet}OH$. Since an excessive amount of $^{\bullet}OH$ leads to the overoxidation of CH_4, it is essential to establish the optimized experimental condition in order to increase the selectivity of the desired products.

In the presence of H_2O_2 under mild conditions (below 100 °C), (i) iron-based catalysts (*e.g.*, single iron atoms confined in graphene,[92] ferric chloride ($FeCl_3$),[93] Fe–Cu-ZSM-5,[94] Fe/ZSM-5,[95,96] Fe/Fe_3C,[35] N-doped carbon supported iron species,[97] *etc.*), (ii) atomic metals or metal nanoparticles embedded/loaded on metal oxides (*e.g.*, single atomic Rh/ZrO_2,[98] AuPd/TiO_2,[99] single atomic Cr/TiO_2,[100] Rh/CeO_2,[101] single atomic Cu/C_3N_4,[102] *etc.*), and (iii) bimetallic materials (*e.g.* Pd@Pt core–shell nanoparticles,[103] Au–Pd alloys,[104] $AuPd_x$ colloids,[105] *etc.*) have been investigated for the partial oxidation of CH_4. For example, graphene-confined single Fe sites (FeN_4/graphene nanosheets (GNs)) (Fig. 16a) effectively oxidized CH_4 to C1 oxygenated products including CH_3OH, CH_3OOH, $HOCH_2OOH$, and HCOOH in the liquid phase, whose turnover frequency (TOF) reached to 0.47 h^{-1} at room temperature.[92] The labelling experiment using $^{13}CH_4$ revealed that C1 oxygenated products were originated from the partial oxidation process instead of the self-oxidation of graphene (Fig. 16b). As the Fe content increased from 1.5 to 4.0 wt%, the yield of C1-oxygenated products increased from 27 to 100 μmol; however, the turnover number (TON) peaked at 2.7 wt% Fe and then decreased with Fe wt%. While more active sites emerged with the increase in the Fe content, the agglomeration among excess Fe species adversely affected the catalytic performance. Besides, with longer reaction time, the C1-oxygenated products were prone to mineralization into CO_2. Under the optimized conditions, the selectivity of C1-oxygenated products and CO_2 was 94 and 6%, respectively. Based on *in operando* time-of-flight mass spectrometry (TOF-MS) data, it was confirmed that the formation of CH_3OH and CH_3OOH was predominant in the first 300 min, whereas $HOCH_2OOH$ and HCOOH markedly increased in the last 300 min (Fig. 16c). The DFT calculation supports that the active oxygen atom can be easily formed by the adsorption and decomposition of H_2O_2 on the Fe site (Fig. 16d). The methyl radical generated through CH_4 activation over O–FeN_4–O would attack the hydroxide and hydroperoxide groups, which produced CH_3OH and CH_3OOH, and the further oxidation of CH_3OH allowed to form $HOCH_2OOH$ and HCOOH (Fig. 16e). As $FeCl_3$ was utilized as a homogenous catalyst in the presence of H_2O_2, the yield of CH_3OH and HCO_2H was recorded as 1.97 and 33.3 mmol g_{cat}^{-1} with a TOF of 5.7 h^{-1}, respectively.[93] It was proposed that the hydrated ferryl ion, $[(H_2O)_5Fe^{IV}O]^{2+}$, that originated from the reaction with H_2O_2 (*i.e.*, $Fe^{3+} + H_2O_2 \rightarrow [Fe^{IV}O]^{2+} + {}^{\bullet}OH + H^+$ or $Fe^{2+} + H_2O_2 \rightarrow [Fe^{IV}O]^{2+} + H_2O$) led to the activation of CH_4 and consequently the formation of CH_3OH. On the other hand, $^{\bullet}OH$ provided by the Fenton process brought about the production of HCO_2H, CO, and CO_2.

On irradiating UV light with a wavelength below 380 nm, the direct photolysis of H_2O_2 drove the formation of $^{\bullet}OH$, which promoted the oxidation of CH_4 to CH_3OH and HCO_2H.[33] With an excess amount of H_2O_2, the consumption of $^{\bullet}OH$ by H_2O_2 ($H_2O_2 + {}^{\bullet}OH \rightarrow {}^{\bullet}OH_2 + H_2O$; $^{\bullet}OH_2 + {}^{\bullet}OH \rightarrow O_2 + H_2O$) decreased the CH_4 conversion. Although the overoxidation of CH_4 was inevitable, the complete mineralization to CO_2 was significantly retarded by establishing the steady state condition that H_2O_2 was added at a constant and relatively low rate. To overcome the drawback, especially a need for energy-intensive UV light and low quantum yield, the activation of H_2O_2 on diverse photocatalysts (*e.g.*, WO_3,[49,53] g-C_3N_4,[47] TiO_2,[34] iron clusters anchored on carbon aerogel,[106] and $BiVO_4$ [55]) and its correlation with the oxidation of CH_4 has been carried out. Under simulated solar light irradiation, the system containing TiO_2, Fe^{2+}, and H_2O_2 transformed CH_4 to CH_3OH, whose yield and selectivity reached up to 471 μmol g^{-1} h^{-1} and 83%, respectively.[34] The conduction and valence band energy levels of TiO_2 are suitable for the redox reaction of ferric/ferrous ions and the formation of $^{\bullet}OH$ by virtue of either water oxidation or H_2O_2 activation (Fig. 17a). Compared with the cases (*e.g.*, TiO_2 + Fe^{2+} + light; $TiO_2 + H_2O_2$ + light; $Fe^{2+} + H_2O_2$), a higher yield and selectivity toward CH_3OH was achieved (Fig. 17b). The screening test using $K_2Cr_2O_7$, *para*-quinone, salicylic acid, and $Na_2C_2O_4$ as scavengers of e^-, $O_2^{\bullet-}$, $^{\bullet}OH$, and h^+, respectively, supports (i) the regeneration of Fe^{2+} is induced by the electron

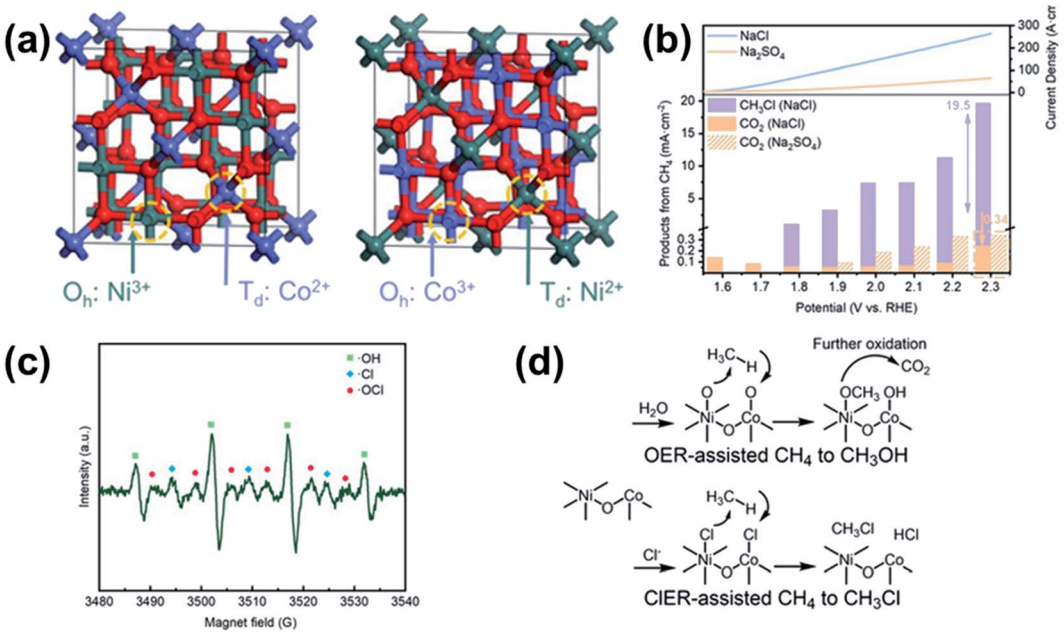

Fig. 18 (a) Co–Ni mixed spinel structures consisting of $CoNi_2O_4$ (left) and Co_2NiO_4 (right). (b) LSV curve (upper panel) and partial current density for products in 0.5 M Na_2SO_4 and saturated NaCl (lower panel). (c) *In situ* EPR spectrum collected using DMPO as a radical capture reagent in electrocatalysis. (d) Different mechanism of CH_4 oxidation in terms of ClER (upper panel) and OER (lower panel). Reproduced with the permission.[109] Copyright 2021, Wiley.

transfer, (ii) the activation of H_2O_2 produces ROS, and (iii) the oxidation of CH_4 proceeds through photogenerated holes and ROS (Fig. 4c and 17c).

The positively charged iron clusters anchored on 3D porous carbon aerogel, denoted as 0.75FeCA800-4, has a good activity for the partial oxidation of CH_4 to CH_3OOH. The 3D porous carbon aerogel with a high electrical conductivity is a good support; therefore, iron clusters with size from 0.25 to 0.45 nm were uniformly dispersed (Fig. 17d). Under simulated solar light irradiation, the production rate and selectivity toward CH_3OOH were 13.2 mmol g_{Fe}^{-1} h^{-1} and almost 100% in the presence of H_2O_2 (2 mmol), respectively (Fig. 17e). The trend that an excess amount of H_2O_2 significantly cut down the selectivity owing to the overoxidation of CH_3OOH to CO_2 was also observed. The *in situ* DRIFTS and *in situ* EPR are powerful tools to understand the real-time reaction mechanism during photocatalysis. As seen in Fig. 17f, new peaks observed at 1306/1348, 1453, and 1550 cm^{-1}, assigned to *C–H, *C–O, and *CH_3–O groups, respectively, increased with the irradiation time. Indeed, Fig. 17g demonstrates that the intensity of both the high spin state $Fe^{\delta+}$ at 200 G and the low spin state $Fe^{\delta+}$ at 3750 G was markedly enhanced with the irradiation time, which indicates that $Fe^{\delta+}$ gave electrons to the carbon atoms. The proposed mechanism is as follows: (i) photoexcitation of carbon atoms in 0.75FeCA800-4, (ii) electron transfer from $Fe^{\delta+}$ to C*, (iii) formation of C^{*-}, (iv) production of CH_4^- *via* the electron transfer from C^{*-} to CH_4, (v) generation of $Fe^{\delta+}$–CH_3* intermediates, (vi) reaction of $Fe^{\delta+}$–CH_3* with ·OH formed by the activation of H_2O_2, (vii) formation of $Fe^{\delta+}$–CH_3O* intermediates, (viii) reaction of $Fe^{\delta+}$–CH_3O* with ·OH, and finally, (ix) the production of CH_3OOH (Fig. 17h).

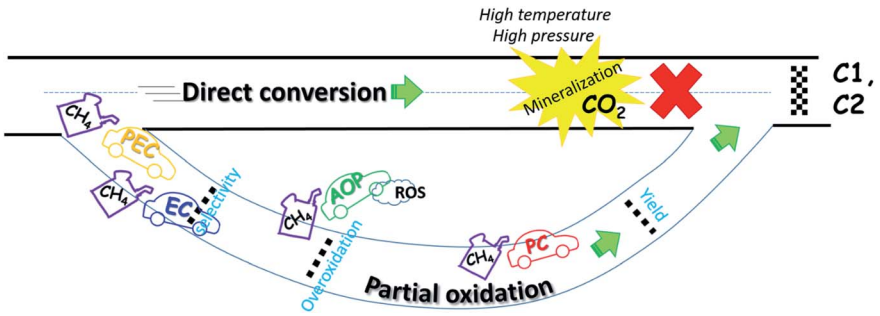

Scheme 1 A schematic representation of photocatalytic (PC), electrocatalytic (EC), photoelectrochemical (PEC), and advanced oxidation process (AOP)-based activation of methane as a tool to detour the energy-intensive process. Partial oxidation processes driven by clean and sustainable technologies are one of the most promising ways to obtain valuable products directly from methane.

The introduction of a relatively excess amount of oxidants and their activation to ROS with high oxidation power may damage the membrane in electrochemical cells. Therefore, oxygen reduction reaction (ORR) catalysts should promote $4e^-$ transfer ($O_2 + 4H^+ + 4e^- \rightarrow 2H_2O$) with suppressed $2e^-$ transfer ($O_2 + 2H^+ + 2e^- \rightarrow H_2O_2$) to be utilized for a proton exchange membrane fuel cell (PEMFC).[107] Although no studies have been reported so far except for one paper, the cathodic activation of H_2O_2 for CH_3OH production in a PEMFC,[108] the recent research work provides a profound insight into the feasibility of producing and handling reactive species for electrocatalytic CH_4 conversion.[109] The cobalt–nickel mixed spinels of Co_2NiO_4 consisting of tetrahedral Ni^{2+} and octahedral Co^{3+} and $CoNi_2O_4$ composed of octahedral Ni^{2+} and tetrahedral Co^{3+} (Fig. 18a) were favorable for generating active chlorine species (*Cl), which promoted the production of CH_3Cl under an applied potential. The surface adsorbed *Cl as an intermediate of the chlorine evolution reaction (CIER) stimulated the cleavage of the C–H bond and overoxidation could be avoided by the release of gaseous CH_3Cl from the electrolyte. In 0.5 M Na_2SO_4 electrolyte, the current density in the LSV curve was quite low due to a high energy barrier, and only CO_2 was evolved (Fig. 18b). However, when an excess amount of Cl^- was present (5.4 M NaCl), the current density at 2.3 V rose up to 19.5 mA cm^{-2} and the CIER-assisted pathway prevailed on the OER-assisted one. The *in situ* EPR experiment confirmed the formation of *Cl and subsequently $^{\bullet}$Cl, where DMPO–Cl$^{\bullet}$, DMPO–OH$^{\bullet}$, and DMPO–OCl$^{\bullet}$ were simultaneously observed (Fig. 18c). Regarding the conversion of CH_4 to CH_3Cl, a higher overpotential to make active oxygen atoms (Ni–O*) is required; thus, the overoxidation of liquid oxygenates is inevitable (Fig. 18d).

4. Conclusions and outlook

Photocatalysis, electrocatalysis, PEC cell, and radical-mediated AOP techniques are capable of bypassing energy-intensive processes (*i.e.*, high temperature and pressure) but are available to utilize the photonic energy (*cf.*, ideally, direct absorption of solar light or PV-powered electrolyzer) as a driving force for the activation of the C–H bond (Scheme 1). The major hurdle of CH_4 partial oxidation refers to (i) low conversion yield of CH_4, (ii) a competitive OER process, (iii) poor selectivity induced by the overoxidation, (iv) mass transfer problem of CH_4 and the final products, (v) separation of the desired products from the electrolytes, (vi) scale-up issue, and (vii) a mysterious reaction mechanism, which should be overcome and verified for practical applications.

Photocatalysis follows a series of processes including (i) photon absorption, (ii) exciton separation, (iii) carrier diffusion, (iv) carrier transport, (v) catalytic efficiency, and (vi) mass transfer of the reactants and products. Therefore, the overall reaction kinetics are governed by the most sluggish step, which means that all the six factors should be optimized in order to increase the photocatalytic activity. In addition, the electronic structure of the photocatalyst (*i.e.*, the bandgap, conduction and valence band position, energy level of the trapping sites for charge carriers, and Fermi level equilibrium) is associated with the thermodynamics that determine whether the reaction proceeds or not. When focusing on not only interfacial charge transfer but also the activation of the C–H bond, the direct dehydrogenation of CH_4 likely proceeds by photogenerated holes over the surface of the photocatalysts. On the other hand, $^{\bullet}$OH provided from the cleavage of *in situ* formed H_2O_2 by electron transfer or hole-mediated water oxidation enables to abstract hydrogen from CH_4 in the proximity of the catalysts. The formation of $^{\bullet}$OH and $O_2^{-\bullet}$ is adjusted by the addition of H_2O_2 or by the reaction under aerobic conditions. The combination of $^{\bullet}CH_3$ with $^{\bullet}$OH produces oxygenates, and the selectivity toward the desired products can be improved by controlling the concentration of $^{\bullet}$OH by suppressing the overoxidation. One of the strategies will be the introduction of a proper scavenger of $^{\bullet}$OH; for example, carbonate (CO_3^{2-}) effectively quenches $^{\bullet}$OH ($k(HCO_3^-) = 8.5 \times 10^6\ M^{-1}\ s^{-1}$ and $k(CO_3^{2-}) = 3.9 \times 10^8\ M^{-1}\ s^{-1}$),[110] resulting in the formation of $CO_3^{\bullet-}$ with a higher standard reduction potential ($E^\circ(CO_3^{\bullet-}/CO_3^{2-}) = 1.63$ V).[111] Likewise, such a high oxidation power of $^{\bullet}$OH would be systematically reduced by electron transfer from the halide ions ($E^\circ(Cl^{\bullet}/Cl^-) = 2.5$ V; $E^\circ(Cl_2^{\bullet-}/Cl^-) = 2.2$ V; $E^\circ(Br^{\bullet}/Br^-) = 2.0$ V; $E^\circ(Br_2^{\bullet-}/Br^-) = 1.7$ V).[112] Another approach is the control of the HOMO and LUMO energy levels in terms of the synthesis and modification of transition metal complexes. Not only the change in the oxidation potential of $^{\bullet}$OH by redox couples but also the emergence of high-valent transition metal ions may assist C–H bond activation and increase the yield and selectivity. Beyond the utilization of H_2O_2, persulfate (peroxymonosulfate and peroxydisulfate), periodate, hypochlorous acid, *etc.*, are also good candidates to supply the radical species through the photocatalytic process. As a non-radical reaction pathway, the influence of singlet oxygen ($^1O_2$) formed *via* the conversion of the singlet excited state to the triplet excited state on the photocatalytic oxidation of CH_4 needs to be proven.

The electrocatalytic partial oxidation of CH_4 to oxygenates under mild conditions is still at quite an early stage, and very limited studies have been undertaken so far. The design of appropriate electrocatalysts and electrochemical cells in consideration of factors such as an electrode configuration, a membrane, an electrolyte, a surrounding condition, *etc.*, is critical to increase the conversion of CH_4 and its selectivity to desired products. In general, high selectivity is achieved at a low current density (*i.e.*, a low conversion yield due to a small number of electrons involved), and as the current density rises, the selectivity significantly decreases due to not only the overoxidation of the target products but also the competitive reaction with OER. To overcome the competitive OER, the development of catalysts with a high Gibbs free energy for water oxidation but with a low one for CH_4 activation is highly required. Under an applied bias, active M–O sites on transition metal oxides promote the dehydrogenation of CH_4, in which the catalyst with a high CH_4 binding energy but a low Madelung potential leads to a higher performance. In the presence of proton acceptors, the deprotonation pathway drives the activation of the C–H bond as well. Therefore, materials that can simultaneously stimulate the dehydrogenation and deprotonation will be favorable for the conversion of CH_4, where more

precise control of the active sites is essential to optimize the selectivity. To better understand the reaction mechanism, real-time spectroscopy is necessary to monitor the change of (i) the oxidation states and electronic structures of transition metal-based catalysts, (ii) reorientation of surface atoms and defects, (iii) electrode surface pH and interaction with electrolyte ions confined in the microenvironment, (iv) the formation of transient species and intermediates, and their correlation with DFT calculation. Through either by the fabrication of MEAs or the modulation of cells by stacking, the size of the device can be scaled-up; thus, the productivity increases to meet the demand of industries. The development of membranes that enable the desired products to be transported from the anode to the cathode chamber, and electrolyte engineering that may help to stabilize oxygenates by solvation (*e.g.*, ionic liquid and H_2SO_4) may effectively retard the overoxidation process. As proposed in photocatalysis and electrocatalysis, the same strategy may be valid to optimize the performance of PEC cells.

The radical-mediated AOP technique looks similar to a double-edged sword because ROS formed by the activation of oxidants accelerate the oxidation of CH_4 but the excess amount drives the complete mineralization into CO_2. Indeed, the prolonged reaction time overoxidizes the desired products. Therefore, the addition of H_2O_2 at regular time intervals to maintain a steady state condition may be more advantageous to reach a higher selectivity. The activation of oxidants into ROS occurs *via* heterogeneous catalysis, whereas the dehydrogenation of CH_4 by ROS is proceeded in the homogeneous phase. Ideally, if ROS are instantaneously produced (*i.e.*, 100% conversion of H_2O_2 to $^{\bullet}OH$ within a few seconds) and the concentration of dissolved CH_4 is enough to consume all $^{\bullet}OH$, overoxidation will be suppressed due to the termination of the radical reaction in the second scale. The concept is quite similar to burst nucleation to synthesize uniform-sized metal nanoparticles.[113] Under atmospheric pressure, micro or nanobubbling of CH_4 would increase the solubility of CH_4 as well as the collision probability of ROS. In order to commercialize the electrocatalytic CH_3OH production directly from CH_4, the conversion efficiency should reach up to 70% by satisfying the operation condition (*i.e.*, cell area $\geq$200 cm^2, current density $\geq$100 mA cm^{-2}, and applied bias $\leq$1 V).[23] Although it may seem like a distinct future when it comes to realization under mild conditions, it is a promising research topic and rapid scientific progress will advance the deployment of self-standing reactors at commercial scales.

Author contributions

Love Kumar Dhandole: investigation, visualization, writing – original draft. Sang Hoon Kim: investigation, writing – original draft. Gun-hee Moon: conceptualization, supervision, writing – review & editing.

Conflicts of interest

There are no conflicts to declare.

Acknowledgements

This research was financially supported by the National Research Foundation of Korea (NRF) funded by the Ministry of Science and ICT (NRF-2020M3H4A3106354), by Korea Environment Industry & Technology Institute (KEITI) through Ecological Imitation-based Environmental Pollution Management Technology Development Project, funded by Korea Ministry of Environment (MOE) (2021002800005), and the KIST internal projects.

Notes and references

1 I. Pérez-Domínguez, A. del Prado, K. Mittenzwei, J. Hristov, S. Frank, A. Tabeau, P. Witzke, P. Havlik, H. van Meijl, J. Lynch, E. Stehfest, G. Pardo, J. Barreiro-Hurle, J. F. L. Koopman and M. J. Sanz-Sánchez, *Nat. Food*, 2021, **2**, 970–980.
2 T. Vandyck, K. Keramidas, A. Kitous, J. V. Spadaro, R. Van Dingenen, M. Holland and B. Saveyn, *Nat. Commun.*, 2018, **9**, 4939.
3 J. J. West, A. M. Fiore, L. W. Horowitz and D. L. Mauzerall, *PNAS*, 2006, **103**, 3988–3993.
4 M. Saunois, A. R. Stavert, B. Poulter, P. Bousquet, J. G. Canadell, R. B. Jackson and e. al, *Earth Syst. Sci. Data*, 2020, **12**, 1561–1623.
5 E. McFarland, *Science*, 2012, **338**, 340–342.
6 R. Horn and R. Schlögl, *Catal. Lett.*, 2015, **145**, 23–39.
7 M. Wang, X. Tan, J. Motuzas, J. Li and S. Liu, *J. Membr. Sci.*, 2021, **620**, 118909.
8 S. D. Angeli, G. Monteleone, A. Giaconia and A. A. Lemonidou, *Int. J. Hydrogen Energy*, 2014, **39**, 1979–1997.
9 M. J. Brown and N. D. Parkyns, *Catal. Today*, 1991, **8**, 305–335.
10 N. J. Gunsalus, A. Koppaka, S. H. Park, S. M. Bischof, B. G. Hashiguchi and R. A. Periana, *Chem. Rev.*, 2017, **117**, 8521–8573.
11 V. N. Cavaliere and D. J. Mindiola, *Chem. Sci.*, 2012, **3**, 3356–3365.
12 Z. Duan and S. Mao, *Geochim. Cosmochim. Acta*, 2006, **70**, 3369–3386.
13 Z. Liang, T. Li, M. Kim, A. Asthagiri and J. F. Weaver, *Science*, 2017, **356**, 299–303.
14 G. Fang, J. Lin and X. Wang, *Chin. J. Chem. Eng.*, 2021, **38**, 18–29.
15 G.-h. Moon, S. Kim, Y.-J. Cho, J. Lim, D.-h. Kim and W. Choi, *Appl. Catal., B*, 2017, **218**, 819–824.
16 P. A. Cook, M. N. R. Ashfold, Y.-J. Jee, K.-H. Jung, S. Harich and X. Yang, *Phys. Chem. Chem. Phys.*, 2001, **3**, 1848–1860.
17 H. Park, H.-i. Kim, G.-h. Moon and W. Choi, *Energy Environ. Sci.*, 2016, **9**, 411–433.
18 W. Kim, T. Tachikawa, G.-h. Moon, T. Majima and W. Choi, *Angew. Chem., Int. Ed.*, 2014, **53**, 14036–14041.
19 J. Y. Hwang, G.-h. Moon, B. Kim, T. Tachikawa, T. Majima, S. Hong, K. Cho, W. Kim and W. Choi, *Appl. Catal., B*, 2021, **286**, 119905.

20 J. C. Fornaciari, D. Primc, K. Kawashima, B. R. Wygant, S. Verma, L. Spanu, C. B. Mullins, A. T. Bell and A. Z. Weber, *ACS Energy Lett.*, 2020, **5**, 2954–2963.
21 K. Liu, W. A. Smith and T. Burdyny, *ACS Energy Lett.*, 2019, **4**, 639–643.
22 S. Yuan, Y. D. Li, J. Y. Peng, Y. M. Questell-Santiago, K. Akkiraju, L. Giordano, D. J. Zheng, S. Bagi, Y. Roman-Leshkov and Y. Shao-Horn, *Adv. Energy Mater.*, 2020, **10**, 2002154.
23 P. Promoppatum and V. Viswanathan, *ACS Sustainable Chem. Eng.*, 2016, **4**, 1736–1745.
24 J. M. Roscoe and M. J. Thompson, 1985, **17**, 967–990.
25 A. V. de Vekki and S. T. Marakaev, *Russ. J. Appl. Chem.*, 2009, **82**, 521–536.
26 X. Meng, X. Cui, N. P. Rajan, L. Yu, D. Deng and X. Bao, *Chem*, 2019, **5**, 2296–2325.
27 R. P. Noceti, C. E. Taylor and J. R. D'Este, *Catal. Today*, 1997, **33**, 199–204.
28 C. E. Taylor, *Catal. Today*, 2003, **84**, 9–15.
29 S. Murcia-López, K. Villa, T. Andreu and J. R. Morante, *ACS Catal.*, 2014, **4**, 3013–3019.
30 W. Zhu, M. Shen, G. Fan, A. Yang, J. R. Meyer, Y. Ou, B. Yin, J. Fortner, M. Foston, Z. Li, Z. Zou and B. Sadtler, *ACS Appl. Nano Mater.*, 2018, **1**, 6683–6691.
31 D. Yu, Y. Jia, Z. Yang, H. Zhang, J. Zhao, Y. Zhao, B. Weng, W. Dai, Z. Li, P. Wang, J. A. Steele, M. B. J. Roeffaers, S. Dai, H. Huang and J. Long, *ACS Sustainable Chem. Eng.*, 2022, **10**, 16–22.
32 K. Villa, S. Murcia-López, T. Andreu and J. R. Morante, *Catal. Commun.*, 2015, **58**, 200–203.
33 Á. López-Martín, A. Caballero and G. Colón, *J. Photochem. Photobiol., A*, 2017, **349**, 216–223.
34 Y. Zeng, H. C. Liu, J. S. Wang, X. Y. Wu and S. L. Wang, *Catal. Sci. Technol.*, 2020, **10**, 2329–2332.
35 Y. Xing, Z. Yao, W. Li, W. Wu, X. Lu, J. Tian, Z. Li, H. Hu and M. Wu, *Angew. Chem., Int. Ed.*, 2021, **60**, 8889–8895.
36 A. Wagner, C. D. Sahm and E. Reisner, *Nat. Catal.*, 2020, **3**, 775–786.
37 G.-h. Moon, M. Yu, C. K. Chan and H. Tüysüz, *Angew. Chem., Int. Ed.*, 2019, **58**, 3491–3495.
38 M. Yu, G. Moon, E. Bill and H. Tüysüz, *ACS Appl. Energy Mater.*, 2019, **2**, 1199–1209.
39 G.-h. Moon, Y. Wang, S. Kim, E. Budiyanto and H. Tüysüz, *ChemSusChem*, 2022, **15**, e202102114.
40 R. S. Rocha, R. M. Reis, M. R. V. Lanza and R. Bertazzoli, *Electrochim. Acta*, 2013, **87**, 606–610.
41 R. S. Kim and Y. Surendranath, *ACS Cent. Sci.*, 2019, **5**, 1179–1186.
42 J. Ma, K. Mao, J. Low, Z. Wang, D. Xi, W. Zhang, H. Ju, Z. Qi, R. Long, X. Wu, L. Song and Y. Xiong, *Angew. Chem., Int. Ed.*, 2021, **60**, 9357–9361.
43 A. Kudo and Y. Miseki, *Chem. Soc. Rev.*, 2009, **38**, 253–278.
44 K. Takanabe, *ACS Catal.*, 2017, **7**, 8006–8022.
45 N. Turro, V. Ramamurthy and A. Scaiano, *Modern Molecular Photochemistry of Organic Molecules*, University Science Books, CA, 2010.
46 K. Villa, S. Murcia-López, J. R. Morante and T. Andreu, *Appl. Catal., B*, 2016, **187**, 30–36.
47 S. Shi, Z. Sun, C. Bao, T. Gao and Y. H. Hu, *Int. J. Energy Res.*, 2020, **44**, 2740–2753.
48 Y. Hu, S. Higashimoto, S. Takahashi, Y. Nagai and M. Anpo, *Catal. Lett.*, 2005, **100**, 35–37.
49 M. A. Gondal, A. Hameed and A. Suwaiyan, *Appl. Catal., A*, 2003, **243**, 165–174.
50 W. Zhou, X. Qiu, Y. Jiang, Y. Fan, S. Wei, D. Han, L. Niu and Z. Tang, *J. Mater. Chem. A*, 2020, **8**, 13277–13284.
51 Y. Hu, Y. Nagai, D. Rahmawaty, C. Wei and M. Anpo, *Catal. Lett.*, 2008, **124**, 80.
52 H.-B. Huang, Z.-B. Fang, K. Yu, J. Lü and R. Cao, *J. Mater. Chem. A*, 2020, **8**, 3882–3891.
53 K. Villa, S. Murcia-López, T. Andreu and J. R. Morante, *Appl. Catal., B*, 2015, **163**, 150–155.
54 S. Wang, L. Wang and W. Huang, *J. Mater. Chem. A*, 2020, **8**, 24307–24352.
55 S. Murcia-López, K. Villa, T. Andreu and J. R. Morante, *Chem. Commun.*, 2015, **51**, 7249–7252.
56 X. Wang, K. Maeda, A. Thomas, K. Takanabe, G. Xin, J. M. Carlsson, K. Domen and M. Antonietti, *Nat. Mater.*, 2009, **8**, 76–80.
57 F. K. Kessler, Y. Zheng, D. Schwarz, C. Merschjann, W. Schnick, X. Wang and M. J. Bojdys, *Nat. Rev. Mater.*, 2017, **2**, 17030.
58 S. Cao, J. Low, J. Yu and M. Jaroniec, *Adv. Mater.*, 2015, **27**, 2150–2176.
59 Y. Li, J. Li, G. Zhang, K. Wang and X. Wu, *ACS Sustainable Chem. Eng.*, 2019, **7**, 4382–4389.
60 J. Xie, R. Jin, A. Li, Y. Bi, Q. Ruan, Y. Deng, Y. Zhang, S. Yao, G. Sankar, D. Ma and J. Tang, *Nat. Catal.*, 2018, **1**, 889–896.
61 X. Chen, Y. Li, X. Pan, D. Cortie, X. Huang and Z. Yi, *Nat. Commun.*, 2016, **7**, 12273.
62 H. Song, X. Meng, S. Wang, W. Zhou, X. Wang, T. Kako and J. Ye, *J. Am. Chem. Soc.*, 2019, **141**, 20507–20515.
63 J. Jang, K. Shen and C. G. Morales-Guio, *Joule*, 2019, **3**, 2589–2593.
64 Q. Wang, M. Kan, Q. Han and G. Zheng, *Small Struct.*, 2021, **2**, 2100037.
65 S. Xie, S. Lin, Q. Zhang, Z. Tian and Y. Wang, *J. Energy Chem.*, 2018, **27**, 1629–1636.
66 M. S. A. Sher Shah, C. Oh, H. Park, Y. J. Hwang, M. Ma and J. H. Park, *Adv. Sci.*, 2020, **7**, 2001946.
67 J. Baltrusaitis, I. Jansen and J. D. Schuttlefield Christus, *Catal. Sci. Technol.*, 2014, **4**, 2397–2411.
68 T. Shi, D. Sridhar, L. Zeng and A. Chen, *Electrochem. Commun.*, 2022, **135**, 107220.
69 Y. Zhang, J. Li and N. Kornienko, *Chem. Commun.*, 2021, **57**, 4230–4238.
70 H. J. Yin, Y. H. Dou, S. Chen, Z. J. Zhu, P. R. Liu and H. J. Zhao, *Adv. Mater.*, 2020, **32**, 1904870.
71 R. F. B. de Souza, D. Z. Florio, E. Antolini and A. O. Neto, *Catalysts*, 2022, **12**, 217.
72 D. Richard, Y.-C. Huang and C. G. Morales-Guio, *Curr. Opin. Electrochem.*, 2021, **30**, 100793.

73 A. G. Abdelkader Mohamed, S. A. Zahra Naqviab and Y. Wang, *ChemCatChem*, 2021, **13**, 787–805.
74 A. Prajapati, B. A. Collins, J. D. Goodpaster and M. R. Singh, *PNAS*, 2021, **118**, e2023233118.
75 Y. Kang, Z. Li, X. Lv, W. Song, Y. Wei, X. Zhang, J. Liu and Z. Zhao, *J. Catal.*, 2021, **393**, 20–29.
76 M. J. Boyd, A. A. Latimer, C. F. Dickens, A. C. Nielander, C. Hahn, J. K. Nørskov, D. C. Higgins and T. F. Jaramillo, *ACS Catal.*, 2019, **9**, 7578–7587.
77 M. Ma, B. J. Jin, P. Li, M. S. Jung, J. I. Kim, Y. Cho, S. Kim, J. H. Moon and J. H. Park, *Adv. Sci.*, 2017, **4**, 1700379.
78 Y. Song, Y. Zhao, G. Nan, W. Chen, Z. Guo, S. Li, Z. Tang, W. Wei and Y. Sun, *Appl. Catal., B*, 2020, **270**, 118888.
79 C. Oh, J. Kim, Y. J. Hwang, M. Ma and J. H. Park, *Appl. Catal., B*, 2021, **283**, 119653.
80 Z. Xie, M. Chen, Y. Chen, A. Guan, Q. Han and G. Zheng, *J. Phys. Chem. C*, 2021, **125**, 13324–13330.
81 M. Ma, C. Oh, J. Kim, J. H. Moon and J. H. Park, *Appl. Catal., B*, 2019, **259**, 118095.
82 F. Hahn and C. A. Melendres, *Electrochim. Acta*, 2001, **46**, 3525–3534.
83 J. Nandenha, E. H. Fontes, R. M. Piasentin, F. C. Fonseca and A. O. Neto, *J. Fuel Chem. Technol.*, 2018, **46**, 1137–1145.
84 F. Amano, A. Shintani, K. Tsurui, H. Mukohara, T. Ohno and S. Takenaka, *ACS Energy Lett.*, 2019, **4**, 502–507.
85 Y. W. Phuan, W.-J. Ong, M. N. Chong and J. D. Ocon, *J. Photochem. Photobiol., C*, 2017, **33**, 54–82.
86 L. Kumar Dhandole, H. Hwi Lee, W.-S. Chae, J. Suk Jang and J. Sung Lee, *J. Energy Chem.*, 2022, **65**, 415–423.
87 L. K. Dhandole, P. Anushkkaran, J. B. Hwang, W.-S. Chae, M. Kumar, H.-H. Lee, S. H. Choi, J. S. Jang and J. S. Lee, *Renewable Energy*, 2022, **189**, 694–703.
88 J. H. Kim, D. Hansora, P. Sharma, J.-W. Jang and J. S. Lee, *Chem. Soc. Rev.*, 2019, **48**, 1908–1971.
89 Y.-C. Wu, R.-J. Song and J.-H. Li, *Org. Chem. Front.*, 2020, **7**, 1895–1902.
90 Y. Miao and M. Shao, *Chin. J. Catal.*, 2022, **43**, 595–610.
91 A. Mehmood, S. Y. Chae and E. D. Park, *Catalysts*, 2021, **11**, 1387.
92 X. Cui, H. Li, Y. Wang, Y. Hu, L. Hua, H. Li, X. Han, Q. Liu, F. Yang, L. He, X. Chen, Q. Li, J. Xiao, D. Deng and X. Bao, *Chem*, 2018, **4**, 1902–1910.
93 L. Zhang, Z. Sun, J. Lang and Y. H. Hu, *Int. J. Energy Res.*, 2021, **45**, 2581–2592.
94 C. Hammond, M. M. Forde, M. H. Ab Rahim, A. Thetford, Q. He, R. L. Jenkins, N. Dimitratos, J. A. Lopez-Sanchez, N. F. Dummer, D. M. Murphy, A. F. Carley, S. H. Taylor, D. J. Willock, E. E. Stangland, J. Kang, H. Hagen, C. J. Kiely and G. J. Hutchings, *Angew. Chem., Int. Ed.*, 2012, **51**, 5129–5133.
95 T. Yu, Z. Li, W. Jones, Y. Liu, Q. He, W. Song, P. Du, B. Yang, H. An, D. M. Farmer, C. Qiu, A. Wang, B. M. Weckhuysen, A. M. Beale and W. Luo, *Chem. Sci.*, 2021, **12**, 3152–3160.
96 Á. Szécsényi, G. Li, J. Gascon and E. A. Pidko, *ACS Catal.*, 2018, **8**, 7961–7972.
97 L. Zhang and Y. Lin, *Appl. Catal., A*, 2021, **615**, 118052.
98 Y. Kwon, T. Y. Kim, G. Kwon, J. Yi and H. Lee, *J. Am. Chem. Soc.*, 2017, **139**, 17694–17699.
99 C. Williams, J. H. Carter, N. F. Dummer, Y. K. Chow, D. J. Morgan, S. Yacob, P. Serna, D. J. Willock, R. J. Meyer, S. H. Taylor and G. J. Hutchings, *ACS Catal.*, 2018, **8**, 2567–2576.
100 Q. Shen, C. Cao, R. Huang, L. Zhu, X. Zhou, Q. Zhang, L. Gu and W. Song, *Angew. Chem., Int. Ed.*, 2020, **59**, 1216–1219.
101 S. Bai, F. Liu, B. Huang, F. Li, H. Lin, T. Wu, M. Sun, J. Wu, Q. Shao, Y. Xu and X. Huang, *Nat. Commun.*, 2020, **11**, 954.
102 B. Wu, R. Yang, L. Shi, T. Lin, X. Yu, M. Huang, K. Gong, F. Sun, Z. Jiang, S. Li, L. Zhong and Y. Sun, *Chem. Commun.*, 2020, **56**, 14677–14680.
103 J. Chen, S. Wang, L. Peres, V. Collière, K. Philippot, P. Lecante, Y. Chen and N. Yan, *Catal. Sci. Technol.*, 2021, **11**, 3493–3500.
104 P. K. Sajith, A. Staykov, M. Yoshida, Y. Shiota and K. Yoshizawa, *J. Phys. Chem. C*, 2020, **124**, 13231–13239.
105 Y. Yan, C. Chen, S. Zou, J. Liu, L. Xiao and J. Fan, *Front. Chem.*, 2020, **8**, 252.
106 K. Zheng, Y. Wu, Z. Hu, X. Jiao, L. Li, Y. Zhao, S. Wang, S. Zhu, W. Liu, W. Yan, Y. Sun and Y. Xie, *Nano Lett.*, 2021, **21**, 10368–10376.
107 X. Ren, Y. Wang, A. Liu, Z. Zhang, Q. Lv and B. Liu, *J. Mater. Chem. A*, 2020, **8**, 24284–24306.
108 J. Nandenha, R. M. Piasentin, L. M. G. Silva, E. H. Fontes, A. O. Neto and R. F. B. de Souza, *Ionics*, 2019, **25**, 5077–5082.
109 Q. Wang, T. Li, C. Yang, M. Chen, A. Guan, L. Yang, S. Li, X. Lv, Y. Wang and G. Zheng, *Angew. Chem., Int. Ed.*, 2021, **60**, 17398–17403.
110 G. V. Buxton, C. L. Greenstock, W. P. Helman and A. B. Ross, *J. Phys. Chem. Ref. Data*, 1988, **17**, 513–886.
111 Z. Zuo, Z. Cai, Y. Katsumura, N. Chitose and Y. Muroya, *Radiat. Phys. Chem.*, 1999, **55**, 15–23.
112 K. Zhang and K. M. Parker, *Environ. Sci. Technol.*, 2018, **52**, 9579–9594.
113 J. Park, J. Joo, S. G. Kwon, Y. Jang and T. Hyeon, *Angew. Chem., Int. Ed.*, 2007, **46**, 4630–4660.
114 X.-Y. Lin, J.-Y. Li, M.-Y. Qi, Z.-R. Tang and Y.-J. Xu, *Catal. Commun.*, 2021, **159**, 106346.
115 H. Song, X. Meng, Z.-j. Wang, H. Liu and J. Ye, *Joule*, 2019, **3**, 1606–1636.
116 Y.-Q. Su, J.-X. Liu, I. A. W. Filot, L. Zhang and E. J. M. Hensen, *ACS Catal.*, 2018, **8**, 6552–6559.

